

**Large Eddy Simulation of flow in porous media:
analysis of the commutation error of the double-averaged equations**

W. Sadowski,¹ M. Sayyari,¹ F. di Mare,¹ and H. Marschall²

¹*Chair of Thermal Turbomachines and Aeroengines,*

*Department of Mechanical Engineering, Ruhr University Bochum, Universitätsstr. 150,
Bochum, 44801, Germany*

²*Computational Multiphase Flow, Department of Mathematics,*

*Technical University Darmstadt, Alarich-Weiss-Str. 10, Darmstadt, 64287,
Germany*

(*Electronic mail: wojciech.sadowski@rub.de)

(Dated: 11 May 2023)

The continuum approach employing porous media models is a robust and efficient solution method in the area of the simulation of fixed-bed reactors. This paper applies the double-averaging methodology to refine the continuum approach, opening a way to alleviate its main limitations: space-invariant averaging volume and inaccurate treatment of the porous/fluid interface. The averaging operator is recast as a general space-time filter allowing for the analysis of commutation errors in a classic *Large Eddy Simulation* (LES) formalism. An explicit filtering framework has been implemented to carry out an *a-posteriori* evaluation of the unclosed terms appearing in the *Double-Averaged Navier-Stokes* (DANS) equations, also considering a space-varying filter width. Two resolved simulations have been performed. First, the flow around a single, stationary particle has been used to validate derived equations and the filtering procedure. Second, an LES of the turbulent flow in a channel partly occupied with a porous medium has been realised and filtered. The commutation error at the porous-fluid interface has been evaluated and compared to the prediction of two models. The significance of the commutation error terms is also discussed and assessed. Finally, the solver for DANS equations has been developed and used to simulate both of the studied geometries. The magnitude of the error associated with neglecting the commutation errors has been investigated and an LES simulation combined with a porous drag model was performed. Very encouraging results have been obtained indicating that the inaccuracy of the drag closure overshadows the error related to the commutation of operators.

Keywords: double-averaging; inhomogeneous filtering; commutation errors; LES

I. INTRODUCTION

Commutation error (CE) terms are the result of the mathematical derivation of averaged differential equations. Their presence arises from the commutation of the averaging and differentiation operators. In the framework of *Large Eddy Simulation* (LES) filtering (see Refs. 1–3), they appear when the averaging (or filtering) is inhomogeneous (i.e. the averaging volume changes with space) or when it is applied near the domain boundary (the averaging volume is extended outside the domain). Exploring both of these situations is an important issue also in the context of the continuum description of flows in porous media or particle assemblies. For example, inhomogeneous filtering may be useful when dealing with porous media with highly non-uniform pore size distribution. In such conditions, the commutation error terms can have a measurable contribution, thus, ignoring them may induce a significant simulation error. The present paper aims to derive and introduce CE terms as source terms (effectively eliminating, or correcting, the induced error) in the context of a space-time averaged flow simulation in porous media.

The simulations of reacting gas flows passing over packed beds are challenging from both the geometrical and computational perspectives. Two recent approaches for such flows are: *particle-resolved Simulation* (PRS), where the geometry of each pellet is accurately represented (see e.g.⁴ or⁵), and *homogenised* modelling, where the packed bed is modelled as a porous medium^{6–8}. The PRS is a computationally demanding method, due to the meshing requirements imposed by complex geometries arising inside the packed bed. On top of that, additional complexity is introduced when the flow is turbulent and needs to be either resolved or modelled. We refer the interested reader to the works of Shams *et al.*^{9–15} for an exhaustive review of turbulence modelling approaches for packed beds.

On the other hand, homogenised modelling usually splits the simulation into two distinct regions: the freeboard unobstructed by the particles or pallets and the porous region created from spatial averaging the flow around said particles⁶. The interface between them is often treated in a discontinuous way. In the porous region, the simulation can be coupled with the *Discrete element method* (DEM) to take into account the interactions between particles¹⁶. The effect of the pallets on the flow in the homogenised region is described using drag models such as the Darcy-Forchheimer¹⁷ or Ergun¹⁸ equations.

A typical treatment of the boundary between the two regions is to use a coupling condition ensuring continuity of the flow variables while prescribing a stress jump at the interface¹⁹. This

approach has been extended to include more complex physics, for example, using averaged quantities from the bed²⁰, including radiation fluxes and temperature distribution²¹, or taking into account the velocity of the moving interface²². However, none of the interface models was entirely successful in accounting accurately for the influence of slip velocity and turbulent interactions, without tweaking the empirical model constants. Additionally, a discontinuous approach is difficult to use in geometries where the interface is hard to define exactly.

An alternative is to describe the interface as a continuous transition between the two regions and model the flow using a single two-phased set of equations. Such a set of equations can be obtained through the *Volume Averaging Theory* (VAT)²³. The *Volume Averaged Navier–Stokes* (VANS) equations have been a good starting point for a rigorous derivation of Darcy’s and Forchheimer’s equations, and two-phase porous media flow models^{17,24,25}. In the VAT framework, unclosed terms describing drag forces and dispersion stresses appear as a result of the averaging operation. This derivation enables estimating their values and an in-depth analysis of their effects. The physical conditions, including the description of the interface²⁶, can be described by space- and time-varying parameters like porosity. Ideally, within this approach, the turbulent mixing and other processes at the interface would be embedded in the turbulence closure.

To extend the VAT to moving beds and turbulent flows, the temporal and spatial averaging are used sequentially, leading to the *Double Averaged Navier–Stokes*, or DANS, equations (for an extensive review the reader is reminded to Lage, de Lemos, and Nield²⁷). The main advantage of the DANS equations is that it describes averaged flow properties in time and space^{28,29}, for example, enabling the analysis of the second-order moments³⁰. The movement of the bed is accounted for through the introduction of a space-time porosity ϕ_{VT} . The basis for the definition of the double-average are the averaging volume and time window, V_0 and T_0 respectively, chosen so that the macroscopic variations of the flow parameters (e.g. large-scale velocity fluctuations) are not filtered out. The underlying assumption is that the characteristic dimension of V_0 will be much larger than the dimension of small-scale flow parameters (turbulent eddies, features of porous matrix) but smaller than the characteristic dimension of the whole domain^{23,31}. On the other hand, less consideration was given to the choice of T_0 in literature. Nikora *et al.*²⁹ state that T_0 must be greater than the turbulent time scale but smaller than the scale of changes in the bed structure. Vowinckel *et al.*³² followed this approach to evaluate the double-averaged statistics of the flow over a moving granular assembly. This means that for a stationary porous structure and flow, an infinite averaging time window can be used, similar to the standard average used in the

*Reynolds averaged Navier–Stokes (RANS)*³³ modelling.

This similarity between the DANS approach and turbulence modelling also extends to spatial averaging, which is equivalent to LES filtering. This observation highlights the other advantage of DANS equations, laying in the ability to bridge the description of porous flow with classical time- and space-averaging based turbulence closures. That being said, the filtering scale is usually much smaller in LES than inside the porous region, therefore, such an approach requires, at least formally, a different filter size in different parts of the domain. Having that in mind, deriving such “combined” models requires an in-depth analysis of averaging operators and operations used in the derivation of the equations, both from a mathematical and numerical standpoint. Initial development of the space-varying averaging in the context of VAT was investigated, for example, by Gray³⁴, who assumed a spherical averaging volume and derived modified averaging theorems, *de facto* correcting the commutation errors of the averaging and differentiation operators.

Investigation of commutation errors is also important for explicit averaging the results from particle-resolved simulations. While the usage of the PRS technique is getting more popular, filtered data can be used to develop more accurate drag and turbulence models, potentially free of empirical correlations. One example of such an approach is the evaluation of the momentum balance in the DANS equations for flows over moving river beds done by Vowinckel *et al.*³² or the analysis of the budget of turbulence kinetic energy³⁵ based on the same data. However, no additional consideration was given to the treatment of commutation errors in both studies. A more thorough investigation of the effects of neglecting CEs was presented by Iovieno and Tordella³⁶. The authors developed a procedure of approximating commutation errors numerically and compensating for their effects by including them as source terms. They investigated the effect both numerically and analytically, in both cases, it was shown that neglecting CEs induces errors, which also influence the flow in regions where the filter length is constant. The authors suggested that the filtering procedure is also applicable to explicit filtering³⁶. We use a similar technique to arrive at DANS equations with commutation error treatment as source terms, with a focus on the analytic form of these source terms. Klein and Germano³⁷ studied the effects of commutation error induced by a filter with a size set by a stretched grid, with a fixed stretching factor. They applied the filtering to isotropic turbulence generated as initial data, and to Direct Numerical Simulation (DNS) results of a turbulent channel flow. They used the differential approximation of the filter and a model based on the scale-similarity hypothesis, to correct the CEs, where in all cases, their modelling approach yielded lower errors than when the commutation errors were neglected. We

compare their formulation to CEs computed from an LES of a channel flow over a porous matrix.

The main focus of the present work is to extend the approach developed by Nikora *et al.*²⁹ to achieve the following goals:

1. Recasting the definition of double averaging operation as filtering, determining the requirements for the filtering operator and using it to rederive the DANS equations. Moreover, including a description of commutation errors, allowing for inhomogeneous filtering and accurate treatment of filtering near boundaries.
2. Numerical verification of all derived error terms by *a-priori* testing on a simplified resolved particle simulation.
3. *A-posteriori* analysis of the non-uniform filtering induced commutation error in a fully developed turbulent flow over a porous medium.
4. Initial development of a solver for double-averaged equations, capable of performing scale-resolving simulation coupled with porous drag closure.

This work is arranged as follows. In Section II, we detail the mathematical model used in this paper. We introduce the filtering operator based on superficial averaging and compute the commutation errors arising from filtering the space and time derivatives, in Sections II A and II B respectively. Next, in Section II C, we apply the filtering to Navier–Stokes equations and describe the commutation errors arising from this operation. Following that, in Section III, we specify the numerical approaches used in this work, and we lay the groundwork to develop a solver for the DANS equations. In Section IV, we detail the test cases used to demonstrate the effects of commutation error terms. Further, in Section V, we discuss the results from the simulations. Lastly, we conclude and provide an outlook in Section VI.

II. METHODOLOGY

Various types of averaging operations are known in the context of multiphase and porous media modelling. The most fundamental distinction must be made between superficial and intrinsic average³⁸. The first one is taken in the whole averaging domain, whereas in the latter, the integration domain is restricted to a subset of the space (in case of double-averaging also time) in which fluid is present (see Figure 1). The double-average can be defined as a consecutive time-space average,

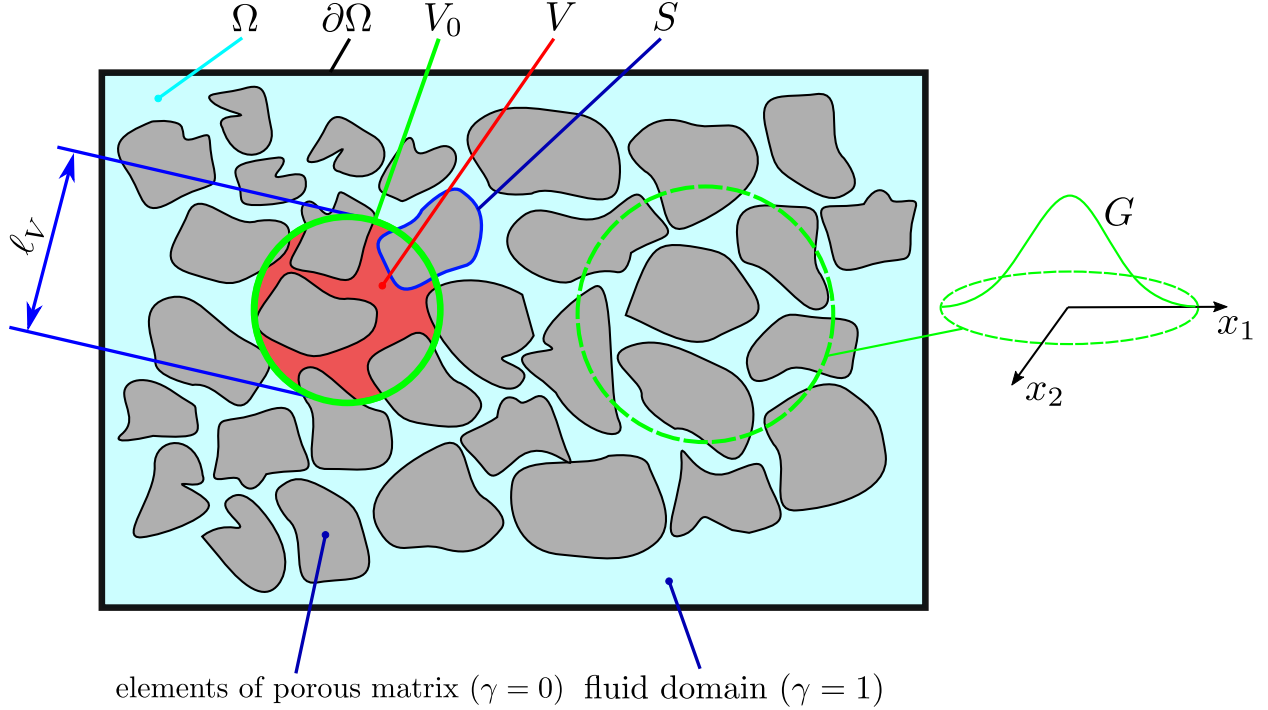


FIG. 1. Schematic description of the porous domain with definitions related to volume averaging/filtering: Ω - the computational domain, $\partial\Omega$ - the boundary of the computational domain, S - the interface between porous matrix elements and fluid, V_0 - averaging volume, V - the volume occupied by the fluid inside the averaging volume, ℓ_V - dimension of the averaging volume/cutoff length scale of the filtering kernel, G - filtering kernel.

averaging in time than in space, the consecutive space-time average or general space-time average where both integrals are applied simultaneously. Intrinsic versions of these averages are not equivalent to each other, however, the superficial space-time average and its consecutive counterparts are all equal, as shown by Nikora *et al.*²⁹. Owing to that, we can restrict our investigation to the analysis of space-time superficial average without any loss of generality.

A. Definition of the filtering operator

A classical description of the double-averaging technique is presented for completeness in Appendix A. Importantly, the main assumption behind the derivation of the averaging theorems is the fact that *the averaging volume remains space-invariant*. To generalise it beyond this constraint and derive the analytical description of the commutation error source terms, we define the filtering operator and write a superficial average based on its kernel.

A space-time filtering kernel G can be defined as a product of time-based kernel $H(t, T_0)$ and a spatial one $\widehat{G}(\mathbf{x}, \ell_V)$, where ℓ_V denotes the characteristic size of \widehat{G} ¹. In the definition of G , both H and \widehat{G} can be arbitrary kernels, provided that they satisfy the following properties. First, $G(\mathbf{x}, t, \ell_V, T_0) = H\widehat{G}$ has to be linear and conserve constants. Second, for consistency, both kernels must approach Dirac δ function in the limit of vanishing filtering width. The superficial average can be written as

$$[\psi]_s(\mathbf{x}, t) = G \star (\gamma\psi) = \int_{-\infty}^{\infty} \int_{\Omega} G(\mathbf{x} - \boldsymbol{\xi}, t - \tau, \ell_V, T_0) \gamma(\boldsymbol{\xi}, \tau) \psi(\boldsymbol{\xi}, \tau) \, d\boldsymbol{\xi} \, d\tau \quad (1)$$

where γ is a clipping or phase indicator function^{29,39} and is equal to 1 in the fluid and 0 in the solid phase. This definition leads to the same formula for space-time porosity as described in Appendix A, i.e. $\phi_{VT} = [1]_s$. Similarly, the superficial average and the space-time porosity ϕ_{VT} are related to the intrinsic average denoted with $[\cdot]$

$$[\psi]_s = \phi_{VT} [\psi]. \quad (2)$$

This allows us to use the double-filtering framework as a generalisation of both spatially and temporally averaged Navier–Stokes equations. When \widehat{G} is assumed to be a spherical top-hat filter and $T_0 = 0$, the standard volume averaging approach is recovered. Similarly, when $\ell_V = 0$ and H is a top-hat filter, the (U)RANS-like average is obtained.

B. Derivation of averaging theorems with commutation errors

Methods used for deriving the averaging theorems are similar to the formulas describing commutation errors in non-homogeneously filtered LES^{1,2}. Merging the approach² and our definition of filtering given by Eq. (1), space-time filtering can be extended to non-homogeneous filters. For this, we introduce a few assumptions guiding this derivation. For simplicity, we consider the cut-off length ℓ_V and time-averaging window T_0 to be dependent only on space, $\ell_V = \ell_V(\mathbf{x})$, and time, $T_0 = T_0(t)$, respectively. Additionally, the extension of the domain occupied by the fluid can change with time, i.e. $\Omega = \Omega(t)$. We define this change by a function $D(\mathbf{x}, t) \in \mathbb{R}^3 \times \mathbb{T}$, equal to 1 in the computational domain $\Omega(t)$ and 0 otherwise (similarly to γ).

The first step in evaluating the commutation error will be taking the derivative of the convolution integral (1) with respect to either x_i or t , which we denote with s as a placeholder. For simplicity, we omit function dependencies since all functions depend on s .

$$\begin{aligned}
\frac{\partial[\psi]_s}{\partial s} &= \frac{\partial}{\partial s} \int_{\Omega(t) \times \mathbb{T}} G\gamma\psi \, d\xi \, d\tau = \frac{\partial}{\partial s} \int_{\mathbb{R} \times \mathbb{T}} G\gamma\psi D \, d\xi \, d\tau \\
&= \int_{\mathbb{R} \times \mathbb{T}} \frac{\partial G\gamma\psi}{\partial s} D \, d\xi \, d\tau + \int_{\mathbb{R} \times \mathbb{T}} G\gamma\psi \frac{\partial D}{\partial s} \, d\xi \, d\tau \\
&= \underbrace{\int_{\Omega(t) \times \mathbb{T}} \frac{\partial G\gamma\psi}{\partial s} \, d\xi \, d\tau}_{=I_1} + \underbrace{\int_{\mathbb{R} \times \mathbb{T}} G\gamma\psi \frac{\partial D}{\partial s} \, d\xi \, d\tau}_{=I_2}.
\end{aligned} \tag{3}$$

The term I_2 in Eq. (3) is related to the error arising when filtering in the bounded domain. Term I_1 can be decomposed into three integrals, after employing the product rule and relations from **C** (assuming here that $s = x_i$).

$$\begin{aligned}
I_1 \Big|_{s=x_i} &= \frac{\partial \ell_V}{\partial x_i} \int_{\Omega(t) \times \mathbb{T}} \frac{\partial G}{\partial \ell_V} \gamma\psi \, d\xi \, d\tau + \int_{\Omega(t) \times \mathbb{T}} G\gamma \frac{\partial \psi}{\partial x_i} \, d\xi \, d\tau + \int_{\Omega(t) \times \mathbb{T}} G n_i \delta(x - \xi - x_S) \psi \, d\xi \, d\tau \\
&= \frac{\partial \ell_V}{\partial x_i} \left\{ \frac{\partial G}{\partial \ell_V} \star (\gamma\psi) \right\} + \int_{S(t) \times \mathbb{T}} G n_i \psi \, d\xi \, d\tau + G \star \left(\gamma \frac{\partial \psi}{\partial x_i} \right).
\end{aligned} \tag{4}$$

The derivatives of D and γ can be treated in the same way. This leads to the following simplification of I_2 term:

$$I_2 \Big|_{s=x_i} = \int_{\partial\Omega(t) \times \mathbb{T}} G\gamma\psi n_i^\Omega \, d\xi \, d\tau \tag{5}$$

Here, n^Ω is the inward normal vector of the domain boundary. After rearranging the terms, the final formula relating the time derivative of the filtered variable and the filtered derivative reads:

$$\left[\frac{\partial \psi}{\partial t} \right]_s = \frac{\partial[\psi]_s}{\partial t} + \int_{S(t) \times \mathbb{T}} G w_i n_i \psi \, d\xi \, d\tau - \frac{\partial T_0}{\partial t} \left\{ \frac{\partial G}{\partial T_0} \star (\gamma\psi) \right\} + \int_{\partial\Omega(t) \times \mathbb{T}} G\gamma\psi w_i^\Omega n_i^\Omega \, d\xi \, d\tau. \tag{6}$$

Similarly, for the space derivative:

$$\left[\frac{\partial \psi}{\partial x_i} \right]_s = \frac{\partial[\psi]_s}{\partial x_i} - \int_{S(t) \times \mathbb{T}} G n_i \psi \, d\xi \, d\tau - \frac{\partial \ell_V}{\partial x_i} \left\{ \frac{\partial G}{\partial \ell_V} \star (\gamma\psi) \right\} - \int_{\partial\Omega(t) \times \mathbb{T}} G\gamma\psi n_i^\Omega \, d\xi \, d\tau. \tag{7}$$

Inspection of the resulting relations leads to the following remarks:

- (i) The integrals over the interface S are identical to the ones presented in equations **(A5)** and **(A6)** (the scaling $1/V_0$ is implicitly included in the filter kernel G).

- (ii) In the limits of homogeneous filtering, the derivatives of ℓ_V over space and T_0 over time vanish. Similarly, on unbounded domains, the boundary terms in equations (6) and (7) also vanish. Then, the equations reduce to equations (A5) and (A6) respectively. This shows that the derived equations are a general form of averaging theorems.
- (iii) The terms containing the derivatives of G describe the error arising when filtering volume is not homogeneous in time and space. This error might be modelled by including those terms in the DANS system. The ensuing error definitions are the generalisation of integrals derived by Gray³⁴ for spherical averaging volume.

The surface integrals over $\partial\Omega(t)$ represent the error arising from filtering near the domain boundary. It should be noted that these have the same form as surface integrals in averaging theorems. Therefore, the boundary can be divided into two parts, $\partial\Omega = \partial\Omega^P + \partial\Omega^C$ where $\partial\Omega^P$ is the part directly adjacent to porous matrix elements and $\partial\Omega^C$ limits the free fluid (boundary surface where $\phi_{VT} = 1$). The term $\partial\Omega^P$, which can be thought of as a rough boundary, can be incorporated into the unclosed source terms (e.g. by extending γ outside the domain assuming $\gamma = 0$) and the commutation error related to this part of the boundary could be fully modelled as a drag force. The surface terms are a generalisation of similar relationships obtained for LES filtering². In the work of Fureby and Tabor², however, an inconsistent choice of the direction of boundary normal vectors with the sign in the expression for $\partial D/\partial x_i$ was made, which has been corrected in the present study.

C. Commutation error terms in the DANS equations

Utilizing the averaging theorems, we analyse the necessary steps to reduce the Navier–Stokes equations using the double-averaging approach discussed in the previous section. We consider the system of the Navier–Stokes equations, assuming isochoric, isothermal and low-mach flows (material properties like density or viscosity remain constant):

$$\begin{cases} \frac{\partial \rho}{\partial t} + \frac{\partial \rho u_j}{\partial x_j} = 0, \\ \frac{\partial \rho u_i}{\partial t} + \frac{\partial \rho u_i u_j}{\partial x_j} = \frac{\partial \sigma_{ij}}{\partial x_j} + \rho f_i, \end{cases} \quad (8)$$

with ρ , \mathbf{u} and \mathbf{f} denoting respectively density, velocity and body forces. The stress tensor is given as $\boldsymbol{\sigma} = -p\mathbf{I} + \mu(\nabla\mathbf{u} + \nabla\mathbf{u}^T)$. The density is kept inside the derivatives on purpose, as

it facilitates the derivation below. In the above equations and throughout the whole paper, the repeated indices imply summation. Application of theorems given by Eq. (A5) and (A6), leads to the Double–Averaged Navier–Stokes system, as defined by Nikora *et al.*²⁹:

$$\frac{\partial \phi_{VT}}{\partial t} + \frac{\partial \phi_{VT}[u_i]}{\partial x_i} = 0, \quad (9a)$$

$$\rho \left(\frac{\partial \phi_{VT}[u_i]}{\partial t} + \frac{\partial \phi_{VT}[u_i][u_j]}{\partial x_j} \right) = \frac{\partial \phi_{VT}[\sigma_{ij}]}{\partial x_j} + \frac{\partial \rho \phi_{VT} \tau_{ij}}{\partial x_j} + \rho \phi_{VT}[f_i] + \rho F_i, \quad (9b)$$

where $\tau_{ij} = [u_i][u_j] - [u_i u_j]$ is the sub-filter stress and \mathbf{F} denotes porous-induced drag force. The derivation of the above system is provided in Appendix B.

Instead, to obtain the commutation error source terms for the DANS equations, we define the filtering with Eq. (1) and apply the generalisations of the averaging theorems, Equations (6) and (7), to the Navier-Stokes system. With this in mind, drag force can be redefined as

$$F_i = - \int_{S(t) \times \mathbb{T}} G \sigma_{ij} n_j \, d\xi \, d\tau$$

and a new DANS system can be formulated. For the momentum equation, the following terms are thus obtained, related to changes of T_0 (10a), change of ℓ_V (10b) and filtering near the boundaries (10c)

$$F_i^{T_0} = \frac{\partial T_0}{\partial t} \left(\frac{\partial G}{\partial T_0} \star (\gamma u_i) \right), \quad (10a)$$

$$F_i^{\ell_V} = \frac{\partial \ell_V}{\partial x_j} \left(\frac{\partial G}{\partial \ell_V} \star (\gamma u_i u_j - \gamma \sigma_{ij}) \right), \quad (10b)$$

$$F_i^\Omega = \int_{\partial\Omega(t) \times \mathbb{T}} G \gamma (-u_i w_j^\Omega + u_i u_j - \sigma_{ij}) n_j^\Omega \, d\xi \, d\tau. \quad (10c)$$

Analogous terms appear for the continuity equation

$$\Lambda^{T_0} = \frac{\partial T_0}{\partial t} \left(\frac{\partial G}{\partial T_0} \star \gamma \right), \quad (11a)$$

$$\Lambda^{\ell_V} = \frac{\partial \ell_V}{\partial x_j} \left(\frac{\partial G}{\partial \ell_V} \star (\gamma u_j) \right), \quad (11b)$$

$$\Lambda^\Omega = \int_{\partial\Omega(t) \times \mathbb{T}} G \gamma (-w_i^\Omega + u_i) n_i^\Omega \, d\xi \, d\tau. \quad (11c)$$

Considering that $F_i^c = F_i^{T_0} + F_i^{\ell v} + F_i^\Omega$ and $\Lambda^c = \Lambda^{T_0} + \Lambda^{\ell v} + \Lambda^\Omega$, the set of corrected double-filtered equations has the following form:

$$\frac{\partial \phi_{VT}}{\partial t} + \frac{\partial \phi_{VT}[u_i]}{\partial x_i} = \Lambda^c, \quad (12a)$$

$$\rho \left(\frac{\partial \phi_{VT}[u_i]}{\partial t} + \frac{\partial \phi_{VT}[u_i][u_j]}{\partial x_j} \right) = \frac{\partial \phi_{VT}[\sigma_{ij}]}{\partial x_j} + \frac{\partial \phi_{VT} \tau_{ij}}{\partial x_j} + \rho (\phi_{VT}[f_i] + F_i + F_i^c). \quad (12b)$$

D. Commutation error terms of the averaged stress tensor

The equations above are very similar to the Navier–Stokes system. However, in order to implement them in the context of a numerical framework (e.g. finite volume formulation), the double-averaged stress tensor $[\sigma]$ needs to be described as a function of averaged velocity. To this aim, it is split into pressure and viscous part

$$\frac{\partial \phi_{VT}[\sigma_{ij}]}{\partial x_j} = -\frac{\partial \phi_{VT}[p]}{\partial x_i} + \frac{\partial [D_{ij}]_s}{\partial x_j}. \quad (13)$$

Using Equation (7) on the viscous stress tensor $[D]_s$ moves the derivatives onto the velocity, generating new unclosed and commutation errors terms:

$$[D_{ij}]_s = \mu \left(\frac{\partial \phi_{VT}[u_i]}{\partial x_j} + \frac{\partial \phi_{VT}[u_j]}{\partial x_i} \right) - D_{ij}^{\ell v} - D_{ij}^S - D_{ij}^\Omega \quad (14)$$

where tensors $D^{\ell v}$, D^S , D^Ω are:

$$D_{ij}^{\ell v} = \mu \left\{ \frac{\partial \ell_V}{\partial x_j} \left(\frac{\partial G}{\partial \ell_V} \star (\gamma u_i) \right) + \frac{\partial \ell_V}{\partial x_i} \left(\frac{\partial G}{\partial \ell_V} \star (\gamma u_j) \right) \right\}, \quad (15a)$$

$$D_{ij}^S = \mu \int_{S(t) \times \mathbb{T}} G(u_i n_j + u_j n_i) \, d\xi \, d\tau, \quad (15b)$$

$$D_{ij}^\Omega = \mu \int_{\partial \Omega(t) \times \mathbb{T}} G \gamma (u_i n_j^\Omega + u_j n_i^\Omega) \, d\xi \, d\tau. \quad (15c)$$

Inserting the above into the momentum equation and writing $D^c = D^{\ell v} + D^\Omega$, results in:

$$\begin{aligned} \rho \left(\frac{\partial \phi_{VT}[u_i]}{\partial t} + \frac{\partial \phi_{VT}[u_i][u_j]}{\partial x_j} \right) &= -\frac{\partial \phi_{VT}[p]}{\partial x_i} + \frac{\partial}{\partial x_j} \left\{ \mu \left(\frac{\partial \phi_{VT}[u_i]}{\partial x_j} + \frac{\partial \phi_{VT}[u_j]}{\partial x_i} \right) \right\} \\ &+ \frac{\partial \phi_{VT} \tau_{ij}}{\partial x_j} + \rho (\phi_{VT}[f_i] + F_i + F_i^c) - \frac{\partial D_{ij}^S}{\partial x_j} - \frac{\partial D_{ij}^c}{\partial x_j}, \end{aligned} \quad (16)$$

which is the form with all of the commutation errors included.

For the cases presented in this work, the obstacles building up the porous medium are stationary, hence the porosity field is constant in time. In that case, we may simplify the momentum and continuity equation. To make the notation clearer, we define $\phi \equiv \phi_{VT}$ and given the isochoric conditions, we incorporate the density into the pressure variable. Due to the no-slip condition at S , $\mathbf{D}^S = \mathbf{0}$. We also decompose the pressure gradient and viscous stress tensor:

$$\frac{\partial \phi[p]}{\partial x_i} = \phi \frac{\partial [p]}{\partial x_i} + [p] \frac{\partial \phi}{\partial x_i}, \quad (17)$$

$$\mathbf{v} \left(\frac{\partial \phi[u_i]}{\partial x_j} + \frac{\partial \phi[u_j]}{\partial x_i} \right) = \phi \mathbf{v} \left(\frac{\partial [u_i]}{\partial x_j} + \frac{\partial [u_j]}{\partial x_i} \right) + \mathbf{v} \left(\frac{\partial \phi}{\partial x_j} [u_i] + \frac{\partial \phi}{\partial x_i} [u_j] \right). \quad (18)$$

The term $\tilde{\mathbf{F}}$ groups all source terms present in momentum equations, apart from the drag force

$$\tilde{\mathbf{F}}_i = \phi [f_i] + F_i^c - \frac{\partial D_{ij}^c}{\partial x_j} + \frac{\partial}{\partial x_j} \left\{ \mathbf{v} \left(\frac{\partial \phi}{\partial x_j} [u_i] + \frac{\partial \phi}{\partial x_i} [u_j] \right) \right\}, \quad (19)$$

resulting in a following DANS system

$$\frac{\partial \phi[u_i]}{\partial x_i} = \Lambda^c \quad (20a)$$

$$\phi \frac{\partial [u_i]}{\partial t} + \frac{\partial \phi[u_i][u_j]}{\partial x_j} = \frac{\partial \phi[p]}{\partial x_i} + \frac{\partial}{\partial x_j} \left\{ \phi \mathbf{v} \left(\frac{\partial [u_i]}{\partial x_j} + \frac{\partial [u_j]}{\partial x_i} \right) \right\} + \frac{\partial \phi \tau_{ij}}{\partial x_j} + F_i + \tilde{\mathbf{F}}_i. \quad (20b)$$

III. NUMERICAL METHOD

In this section, we describe the numerical methods and their setup for the test cases studied in the paper. Additionally, we discuss the schemes used in PRSs, the choice of filter, and the DANS solver.

A. Explicit filtering of PRS

The fields computed in the PRSs were filtered to arrive at the double-averaged quantities. The filtering is done using the postprocessing utility described and validated in our previous work⁴⁰. To ensure consistent results across different spatial kernels, each kernel must be scaled properly. This is achieved using the condition

$$\ell_V^N = \int_{\Omega} \frac{\widehat{G}(\mathbf{x}, \ell_V)}{\widehat{G}(\mathbf{0}, \ell_V)} d\mathbf{x}, \quad (21)$$

where N is the dimensionality of the considered domain. We also restrict ourselves to C^0 kernels, as any discontinuities would be inaccurately reproduced on the general unstructured mesh, introducing an error in the filtering process (e.g. the filter will not preserve constants).

In this work, two filters were considered, a Gaussian kernel, and a so-called Cellular kernel. The Gaussian filter is given by

$$\widehat{G}_G = \frac{1}{\ell_V^{N/2}} \exp\left(-\pi x_i x_i / \ell_V^2\right), \quad (22)$$

with N denoting the dimensionality of the domain. Whereas the Cellular kernel, introduced in⁴¹, is defined in one spatial dimension as

$$\widehat{G}_C = \frac{\ell_V - |x|}{\ell_V^2}. \quad (23)$$

For a spatially periodic porous medium, the cellular filter can be generalized to three-dimensions by multiplying the filters representing each dimension^{41,42}.

To evaluate the commutation errors related to the change of ℓ_V , the derivative $\partial \widehat{G} / \partial \ell_V$ has to be evaluated. In the present work, only Gaussian kernel will be considered in this context and its derivative is computed as

$$\frac{\partial \widehat{G}_G}{\partial \ell_V} = -\frac{1}{2\ell_V^3} \left(N\ell_V^2 - 4\pi x_i x_i \right) \widehat{G}_G. \quad (24)$$

To speed up both filtering and computing the distributions of \widehat{G} , the kernel distribution can be clipped to 0 after a certain distance d from the center of filtering molecule. We restrict this clipping such that the error of filtering operation introduced by clipping is less than 1%, i.e. the integral of the clipped kernel is at least equal to 0.99. A similar procedure can be followed when using $\partial \widehat{G} / \partial \ell_V$. However, here the measurement of error is less straightforward as the integral of the derivative of the kernel is by definition equal to 0:

$$\int_{\Omega} \frac{\partial \widehat{G}}{\partial \ell_V} d\mathbf{x} = \frac{\partial}{\partial \ell_V} \int_{\Omega} \widehat{G} d\mathbf{x} = \frac{\partial 1}{\partial \ell_V} = 0. \quad (25)$$

Therefore, a sensitivity study was conducted on the influence of the clipping distance for the accuracy of computed quantities based on the filtering of results from G1 test case (see **IV** for description of the geometry and setup). It is presented in **D**. Both Gaussian kernel and its derivative have been clipped at $d/\ell_V = 1.8$.

B. Modelling and approximation of the commutation errors

Filtering operation with any well defined kernel can be approximated by solving following differential equation¹:

$$\langle \psi \rangle^G - \frac{\alpha_2}{2} \frac{\partial^2 \langle \psi \rangle^G}{\partial x^2} \approx \psi. \quad (26)$$

In the above equation we denote an intrinsically filtered quantity with the brackets $\langle \cdot \rangle^G$. For simplicity we assume that the filtering occurs only in space and filter is only one dimensional, i.e. $G = G(\ell_V, x)$. Additionally, α_2 , denotes second moment of the chosen kernel, given as:

$$\alpha_2 = \int_{\Omega} \xi^2 G(\ell_V, \xi) d\xi. \quad (27)$$

Differentiating (26) w.r.t. filter width, an approximation for the convolution product $(\partial G / \partial \ell_V) \star \psi$ can be derived:

$$\frac{\partial G}{\partial \ell_V} \star \psi \approx \frac{1}{2} \frac{\partial \alpha_2}{\partial \ell_V} \frac{\partial^2 \langle \psi \rangle^G}{\partial x^2}. \quad (28)$$

In our case, for both kernels (22) and (23), α_2 is equal to $\ell_V^2/6$:

$$\frac{\partial G}{\partial \ell_V} \star \psi \approx \frac{\ell_V}{6} \frac{\partial^2 \langle \psi \rangle^G}{\partial x^2}. \quad (29)$$

Klein and Germano³⁷ have reported that the above approximation performs quite well based on the tests on the DNS data. They have also attempted modeling of the error using the scale similarity hypothesis¹. The commutation error term can be expressed as

$$\frac{\partial \ell_V}{\partial x} \left(\frac{\partial G}{\partial \ell_V} \star \psi \right) \approx C \tau_G(\partial_x, \langle \psi \rangle^G) = C \left(\left\langle \frac{\partial \langle \psi \rangle^G}{\partial x} \right\rangle^G - \frac{\partial \langle \langle \psi \rangle^G \rangle^G}{\partial x} \right), \quad (30)$$

where $\tau_G(\partial_x, \langle \psi \rangle^G)$ denotes *Generalised Central Moment* (GCM) associated with $\langle \partial \langle \psi \rangle^G / \partial x \rangle^G$. The coefficient C is of the order of one. Alternatively, a model by Bardino, Ferziger, and Reynolds⁴³ can be used to determine C dynamically, using two filter levels. Given a second filtering operation, denoted here with $\langle \cdot \rangle^F$, which corresponds to a kernel $F = G(2\ell_V, x)$, GCM can also be defined for a quantity filtered with both kernels (described as $\langle \psi \rangle^{GF} \equiv \langle \langle \psi \rangle^G \rangle^F$ for brevity):

$$\tau_{GF}(\partial_x, \langle \psi \rangle^{GF}) = \left\langle \frac{\partial \langle \psi \rangle^{GF}}{\partial x} \right\rangle^{GF} - \frac{\partial \langle \langle \psi \rangle^{GF} \rangle^{GF}}{\partial x}, \quad (31)$$

and similarly

$$\tau_F(\partial_x, \langle \psi \rangle^G) = \left\langle \frac{\partial \langle \psi \rangle^G}{\partial x} \right\rangle^F - \frac{\partial \langle \langle \psi \rangle^G \rangle^F}{\partial x}. \quad (32)$$

Finally, value of C can be computed as

$$C = \frac{\tau_F(\partial_x, \langle \Psi \rangle^G) I}{I^2}, \quad I = \tau_{GF}(\partial_x, \langle \Psi \rangle_{GF}) - \langle \tau_G(\partial_x, \langle \Psi \rangle_G) \rangle^F. \quad (33)$$

C. PIMPLE algorithm for DAND equations

As mentioned before, considered test cases, will be simulated using filtered equations. Since the solid elements are stationary for both configurations, we can assume that porosity does not depend on time. With this, we restrict our simulation to the system (20).

Focusing first on the unsteady simulation of the channel and following Breugem⁴², we assume following closure for the drag term

$$F_i \approx -\frac{\partial \phi}{\partial x_j} \left\{ -[p] \delta_{ij} + \mathbf{v} \left(\frac{\partial [u_i]}{\partial x_j} + \frac{\partial [u_j]}{\partial x_i} \right) \right\} - \mathbf{v} \mathcal{K}^{-1} (1 + \mathcal{F}) \phi^2 [u_i]. \quad (34)$$

Where the first term on the right-hand side is meant to simplify the momentum equation, according to the estimations by Quintard and Whitaker⁴¹ and the last defines the standard Darcy-Forchheimer drag model²³.

Assuming that the porous medium has the form of an array of cubes, the model coefficients can be computed in the following way Irmay⁴⁴. Considering that d_p denotes particle size, here taken to be equal to the dimension of the cube, the inverse of permeability \mathcal{K} is given as

$$d_p^2 \mathcal{K}^{-1} = C_K \frac{1 - \phi}{\left(1 - (1 - \phi)^{1/3}\right)^3 \left(1 + (1 - \phi)^{1/3}\right)}. \quad (35)$$

The Forchheimer coefficient \mathcal{F} can be computed in the following manner:

$$d_p^2 \mathcal{F} \mathcal{K}^{-1} = C_F \left(\frac{1 - \phi}{\phi} \right) \frac{\phi |\mathbf{u}| d_p}{\mathbf{v}}. \quad (36)$$

Breugem, Boersma, and Uittenbogaard⁴⁵ calibrated the model coefficients for a given geometry, resulting in values $C_K \approx 11.4$ and $C_F \approx 0.4$. It is important to note that the choice of the drag model has a big influence on the overall accuracy of the computation. Chosen model is a good representation of an isotropic and fully regular porous matrix as chosen for this analysis, however, when a more complex geometry would be adopted, the model should account for more sophisticated physical effects, e.g. include the influence of non-isotropy. Substituting the Equation (34)

into the Equation (20), leads to a modified momentum equation given by

$$\begin{aligned} \phi \frac{\partial [u_i]}{\partial t} + \frac{\partial \phi [u_i][u_j]}{\partial x_j} = \phi \frac{\partial [p]}{\partial x_i} + \phi \frac{\partial}{\partial x_j} \left\{ \nu \left(\frac{\partial [u_i]}{\partial x_j} + \frac{\partial [u_j]}{\partial x_i} \right) \right\} + \frac{\partial \phi \tau_{ij}}{\partial x_j} \\ + \tilde{F}_i - \nu \mathcal{K}^{-1} (1 + \mathcal{F}) \phi^2 [u_i]. \end{aligned} \quad (37)$$

According to the analysis by Breugem⁴², for turbulent flows in porous media the sub-filter stresses can usually be neglected in the porous region, as the contributions of drag to the momentum balance is greater than the turbulent dispersion. Furthermore, in most cases, it can be assumed that the turbulence is confined to a pore size. This assumption, expressed as the pore scale prevalence hypothesis (PSPH), has been tested in several DNS studies, see for example work by Jin *et al.*⁴⁶. Therefore, if the turbulence does not lead to significant mixing on the macroscopic scale, than there is no need to add any up-scaled dispersion model (e.g. additional viscosity) to the equations. Additionally, a DNS study of the flow over a modelled porous medium by Breugem, Boersma, and Uittenbogaard³⁹ suggests that resolved fluctuations diminish quickly in the porous material. Having that in mind, for LES simulations, we decided to use eddy-viscosity closure for the sub-filter stresses (based on the Boussinesq hypothesis¹) in the whole domain. Based on results from Ref. 39 we assume that the undisturbed, non-fluctuating flow field in the porous region implicitly results in a null sub-grid scale viscosity. The advantage of such an approach is its locality, i.e. the turbulence model remains the same for each region of the flow. The resultant momentum equation (both viscosities are combined into ν_{eff}),

$$\phi \frac{\partial [u_i]}{\partial t} + \frac{\partial \phi [u_i][u_j]}{\partial x_j} = \phi \frac{\partial [p]}{\partial x_i} + \phi \frac{\partial}{\partial x_j} \left\{ \nu_{\text{eff}} \left(\frac{\partial [u_i]}{\partial x_j} + \frac{\partial [u_j]}{\partial x_i} \right) \right\} + \tilde{F}_i - \nu \mathcal{K}^{-1} (1 + \mathcal{F}) \phi^2 [u_i], \quad (38)$$

leads to the semi-discrete equation for velocity similar to the one obtained from the standard incompressible Navier–Stokes equation:

$$a_p[\mathbf{u}]_p = \mathbf{H}([\mathbf{u}]) - \phi \nabla [p]. \quad (39)$$

When interpolated onto faces and inserted into the continuity equation, the standard incompressible Navier–Stokes equation forms the Poisson equation for the pressure⁴⁷:

$$\nabla \cdot \left(\frac{\phi_{VT}^2}{a_p} \nabla [p] \right) = \nabla \cdot \left(\frac{\phi_{VT} \mathbf{H}([\mathbf{u}])}{a_p} \right) - \Lambda^c. \quad (40)$$

Equations (39) and (40) are solved in an identical fashion as in the standard PIMPLE-based OpenFOAM solvers.

The algorithm for the steady state solver is constructed in a similar way, starting again from Equation (20) with the time derivative in the momentum equation set to zero. As mentioned before, instead of models, an accurate representations of unclosed terms, obtained from explicit filtering, is used.

D. Simulations setup

All of the simulations and postprocessing was performed using the OpenFOAM toolbox^{48,49}. For the PRSs, the divergence term has been discretised with the central difference scheme. Stationary computations were carried out with SIMPLE steady-state algorithm^{47,50}. The LES computations were performed with WALE⁵¹ model using the incompressible, pressure-based PIMPLE method. For the time derivative, a second-order accurate backward difference scheme has been used.

To judge the quality of the LES, the ratio of resolved to total *turbulent kinetic energy* (TKE) was used as an indicator, given by

$$M = \frac{\overline{u'_i u'_i}}{(2k_{sgs} + \overline{u'_i u'_i})},$$

where the subgrid-scale contribution was estimated as $k_{sgs} = v_t^2 / (C_k^2 \Delta^2)$, with $C_k = 0.094$. The cell size Δ was computed as a cube root of the cell volume. A proper LES is characterised by resolving more than 80% of the energy spectrum^{52,53}, therefore, time average of M should be greater than 0.8.

In case of the simulations performed with the DANS solver described in III C, the same schemes and models were used for LES as for PRS. In case of steady-state simulations, we do not model the drag or sub-filter stresses, instead, we use accurate values computed from explicit filtering. The convective term was also discretised with second order accurate upwind scheme to ensure stability in the vicinity of sharply rising source terms.

IV. TEST CASES

In the present work, we consider an incompressible flow in two geometries, where both flow fields are simulated and analysed in a similar fashion. In each case, the particle-resolved simulations have been performed and filtered to generate the CEs and other terms arising in double-filtered equations. Both cases have also been simulated assuming that the porous medium is modelled by a porosity distribution. A summary of the cases is provided in Table I.

A. Two-dimensional flow over a square cylinder (G1)

The first test case is a simplified PRS considering two-dimensional, laminar, stationary flow around a square bar, denoted as PRS-G1 in this paper. The geometrical configuration and boundary conditions are shown in Figure 2. A uniform velocity profile is assumed at the inlet. The Reynolds number, based on the square side a and the inlet velocity, is equal to 1. The computational mesh used for this simulation is shown in Figure 3. The cell sizing is progressively refined from $a/10$ in the farfield region to $a/80$ in the boundary layer of the cylinder.

The flow has been filtered three times, resulting in three separate sets of filtered quantities, discussed in detail in Section V A. First, to establish a reference, uniform filter width was chosen resulting in a flow field without the commutation errors. Moreover, averaging was done in a truncated domain to avoid the influence of the boundaries. Second, the filtering domain was expanded to introduce the boundary errors into the equations. Third, using the truncated domain again, inhomogeneous filtering was conducted. Those results sets are named G1-A, G1-B and G1-C respectively.

The particle-resolved simulation requires no additional modelling applied to the Navier-Stokes system, which aids in evaluating the viscous stress and, therefore, the drag term \mathbf{F} exactly. Two-dimensionality simplifies the potentially computationally intensive non-local filtering operation. Lastly, since the definition of the filtering is robust, without a loss of generality we can assume that the width of the time kernel H is infinite. Since consecutive space-time filtering is equivalent to double-filtering and a stationary solution can be seen as time-filtered over an infinite averaging window, we can restrict our investigation to spatial filtering of the stationary solution. Therefore, while conducting inhomogeneous filtering, we assume that the terms \mathbf{F}^{T_0} and Λ^{T_0} are equal to zero.

This flow has also been computed employing the solver described in Section III. Several vari-

TABLE I. Summary of the test cases, filtered data sets and their naming. For the simulations both the geometry (t.d. denotes a simulation conducted in a truncated domain shown in Figure 2 with red lines) and the numerical approach is listed. Additionally, the CE source terms used to compute the flow are reported. The results are compared to the explicitly filtered results datasets from both PRSs. Here employed filter size and type is reported along with evaluated CEs.

Simulations				
Name	Geometry	Approach	CE terms	Additional information
PRS-G1	Figure 2	PRS		2D, laminar, steady flow around square cylinder
PRS-G2	Figure 4	PRS/LES		3D, turbulent, channel with a porous wall
DA-G1-A	Figure 2, t.d.	DANS		G1 geometry, with filtered equations
DA-G1-B	Figure 2	DANS		tests the importance of Eq. (10c), (11c)
DA-G1-C1	Figure 2, t.d.	DANS	$\Lambda^{\ell_V}, \mathbf{F}^{\ell_V}, \mathbf{D}^{\ell_V}$	tests the importance of Eq. (10b), (11b) and (15a)
DA-G1-C2	Figure 2, t.d.	DANS	Λ^{ℓ_V}	
DA-G2-A1	Figure 4	DANS/LES		G2 geometry, drag fully modelled, ℓ_V like below
DA-G2-A2	Figure 4	DANS/LES		
Filtered data sets				
Name	ℓ_V	Kernel	CE terms	Additional information
G1-A	$4\sqrt{\pi/6}a$	Eq. (22)		filtering done in the truncated domain
G1-B	$4\sqrt{\pi/6}a$	Eq. (22)	Λ^b, \mathbf{F}^b	computation of boundary CEs
G1-C	inhomogeneous	Eq. (22)	$\Lambda^{\ell_V}, \mathbf{F}^{\ell_V}, \mathbf{D}^{\ell_V}$	computation of inhomogeneous filtering CEs
G2-A1	$H/10$	Eq. (23)		filtered as in Ref 42
G2-A2	$H/5$	Eq. (23)		tests the influence of filter size vs. G2-B
G2-B	inhomogeneous	Eq. (22)	$\Lambda^{\ell_V}, \mathbf{F}^{\ell_V}$	change of filter size at porous-fluid interface

ants of the simulation have been performed, each focused on testing the importance of different error terms while implementing the equations. In these simulations, the CEs are not being mod-

elled, instead, the fields from results sets A to C are used. The case DA-G1-A aims to reproduce velocity and pressure fields from G1-A and is computed in the same truncated domain. Simulation DA-G1-B was conducted in the full domain and investigates the importance of Λ^b and \mathbf{F}^b terms. Similarly, DA-G1-C1 and C2 test the commutation error terms related to inhomogeneous filtering. The particularities of each setup are described in detail in Section V.

The simulations of DA-G1 test case were conducted on the purely quadrilateral uniform meshes. Cases DA-G1-A1, B1 and B2 had cell size set as $0.08a$ in the horizontal direction and $0.1a$ in the vertical direction. The cases C1 and C2, following the results of the sensitivity study described in Appendix D, were meshed with cell size set to $0.05a$.

B. Turbulent flow in a channel with permeable wall (G2)

The second case considered in the study, is the turbulent flow in an infinitely long planar channel, with the lower section of the geometry occupied by a set of cubes, thereby modelling a sparse packing or porous medium. This case, named PRS-G2, is based on the work of Breugem⁴² who conducted both a particle-resolved and homogenised DNS of this flow. As mentioned in the introduction, if such a configuration is simulated with a porosity-based drag model, it has to be

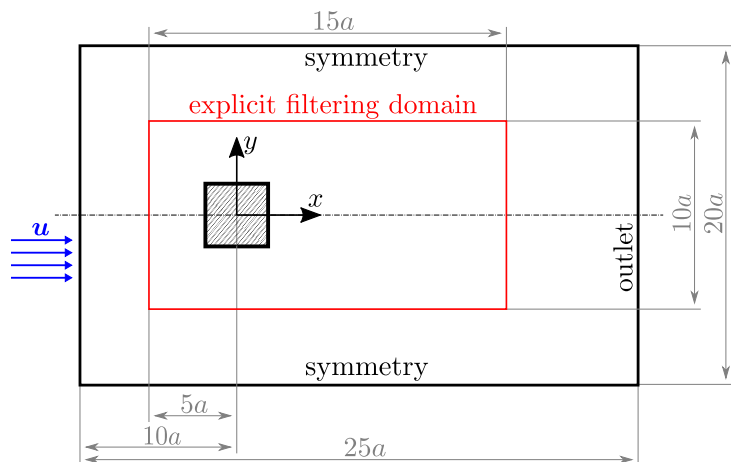


FIG. 2. Schematic depiction of computational geometry and boundary conditions for the PRS-G1 simulation. Red lines denote the truncated domain, used for explicit filtering without commutation error terms and DA-G1-A, C1 and C2 simulations.

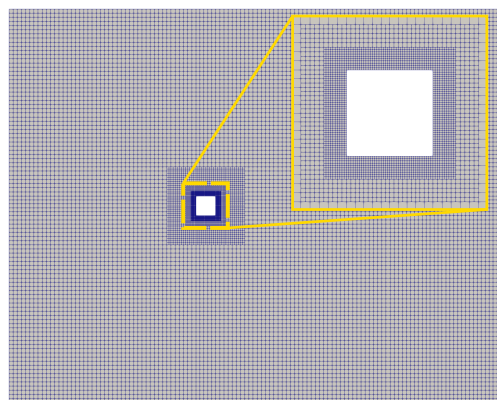


FIG. 3. Computational mesh used in PRS-G1 case. Every second grid line is shown.

“blended” with the standard Navier-Stokes equations. This in turn requires the filter size to change and induces the commutation error. While performing the DNS with a drag model, Breugem⁴² neglected the commutation error. We use his results as a reference, adapt his modelling approach to work in the LES framework and evaluate the commutation error in a more realistic setting: unsteady, turbulent flow.

The geometry of the computational domain is visible in Figure 4. The Reynolds number is defined as $Re_{\text{bulk}} = U_{\text{bulk}}H/\nu = 5500$ (bulk velocity is computed in the channel section $y \geq 0$). The coordinate system is defined in such a way that x is the streamwise dimension, y is wall-normal, and z is spanwise. The channel has dimensions of $3H \times 2H \times 2H$. The domain is periodic in both streamwise and spanwise directions. The cubes have the size of $H/20$. The distance between the centres of the cubes is equal to $H/10$. The first cube’s centre is located $3H/40$ from the bottom wall. There are 9 layers of cubes, leaving the centre of the top layer at $y = -0.125H$. Chosen dimensions of the geometry give the nominal porosity in the bulk $\phi = 0.875$. The flow is driven by a momentum source, prescribing the pressure gradient so that the bulk velocity in the upper part of the channel results in the prescribed Re_{bulk} .

The unsteady fields were time-averaged over the period required for 60 flow-trough times. To further improve the convergence of statistics, the time averaged fields were spatially averaged considering the periodic nature of the computational domain. The geometry contains 600 identical

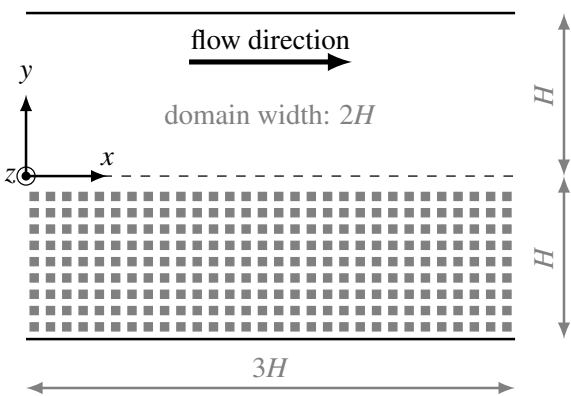


FIG. 4. Schematic depiction of computational geometry for the turbulent flow in the channel with the lower part occupied with porous matrix modelled by a set of cubes.

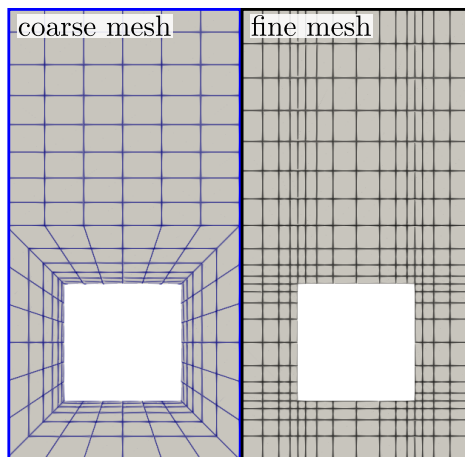


FIG. 5. Detailed view of the computational meshes used for the channel simulation near the last layer of cubes (slice through the middle of the cube). Only one column of cubes is shown for each mesh.

TABLE II. Statistics of the meshes used to conduct the particle-resolved LES of configuration G2. Cell sizes Δ_x^{+t} , Δ_y^{+t} and Δ_z^{+t} are normalised using the friction velocity computed at the top wall of the channel, u_τ^t .

mesh	coarse	fine
number of cells	8 467 200	29 952 000
max non-orthogonality angle	50°	0°
max skewness	2.5	0
max x^+, y^+, z^+	8.6, 0.7, 8.6	7.8, 1.4, 6.1
clear channel $\Delta_x^{+t}, \Delta_y^{+t}, \Delta_z^{+t}$	6.5, 0.65-15.3, 6.5	1.3-4, 0.55-7.67, 1.3-4

sections, repeated in x and z directions, consisting of a column of cubes and a channel section on top.

The computations on two different meshes have been realised to ensure a proper resolution of both the turbulent flow field and the stress tensor at the walls of the cubes. The latter is of great importance, as the values at the surfaces will contribute directly to the computation of the drag force using explicit filtering. Both meshes, the coarse and the fine one, are visible in Figure 5. The statistics of the meshes are also presented in Table II.

According to Chapman⁵⁴, to obtain an appropriate representation of structures inside the boundary layer, the wall spacing needs to fulfil the requirements $x^+ < 100$, $y^+ < 2$, and $z^+ < 20$. Both of the considered meshes, fulfil these criteria.

The resolved fields have been filtered with both Cellular and Gaussian kernels, Equations (23) and (22) respectively. Results from filtering with the first are used to validate the simulation against Ref 42. The latter is employed to investigate the CE, due to the smoothness of the $\partial\hat{G}/\partial\ell_V$ function, given by Equation (24). Since the time-filtering kernel assumes an infinite time scale, only the commutation errors related to spatial filtering were considered.

The flow in a channel was also computed with the implemented solver. The simulations (named DA-G2-A and B) were performed assuming two different filter sizes inside the packing, $\ell_V = H/10$ and $\ell_V = H/5$, resulting in two different porosity distributions in the channel $\phi(y)$ given by:

$$y \in (\delta^-, \delta^+) : \quad \frac{\phi(y)}{\phi^+ - \phi^-} = 6 \left(\frac{y - \delta^+}{\delta^+ - \delta^-} \right)^5 + 15 \left(\frac{y - \delta^+}{\delta^+ - \delta^-} \right)^4 + 10 \left(\frac{y - \delta^+}{\delta^+ - \delta^-} \right)^3 + \frac{\phi^+}{\phi^+ - \phi^-}. \quad (41)$$

Porosity over the bed, $y \geq \delta^+$, denoted as ϕ^+ is equal to 1. In the porous region, for $y \leq \delta^-$, it is given as $\phi^- = 0.875$. For $\ell_V = H/10$ the porosity changes in the region $(\delta^-, \delta^+) = (0.075H, 0)$, whereas in case of $\ell_V = H/5$ it changes over $(-0.25H, 0.1H)$. The profiles of the porosities are depicted in Figure 6. They provide a very good approximation of ϕ resulting from the filtering procedure.

The dimensions of the domain remain the same as in the particle-resolved simulation. The flow is also driven by a pressure gradient updated to ensure the correct Re_{bulk} . The drag closure used for these configurations and equations used in both simulations is described in Section III.

Because the cases DA-G2-A and B employ LES as the turbulence modelling strategy, we assume that the time filtering kernel is reduced to the δ function. We can further assume that the spatial filter is connected to the mesh size in the clear fluid region, $\phi = 1$. On the other hand, in the porous region, we only assume spatial filtering with the $\ell_V = H/10$ or $\ell_V = H/5$.

To reach the double-averaged description of flow parameters, the solutions have been additionally time averaged across 60 flow-through times. To further boost collected statistics, the flow field can be averaged in homogeneous directions.

The simulations have been performed on fully hexahedral and orthogonal meshes, refined near the walls and interface region. For each case, two mesh resolutions were tested to assess the influence of mesh resolution on the results. The statistics of the meshes are listed in Table III. LES

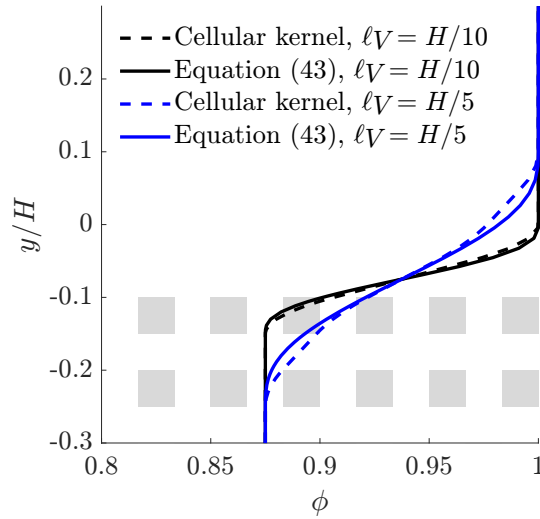


FIG. 6. Distributions of porosity in DA-G2-A and B simulations (for two different filter sizes), compared to curves computed by explicit filtering with Cellular kernel.

TABLE III. Statistics of the meshes used for simulation of the G2 case with the double-averaged equations. Cell sizes are normalised by the friction velocity at the top wall of the channel u_τ^t . The last column describes the wall-normal cell dimension in the area where porosity changes.

mesh & ℓ_V	number of cells	$\Delta_x^{+t}, \Delta_y^{+t}, \Delta_z^{+t}$	interface Δ_y^{t+}
coarse & $H/10$	600000	8, 0.4-13.6, 15.5	3.5
coarse & $H/5$	600000	8, 0.4-14, 16	3.6
fine & $H/10$	2700000	8, 0.2-6, 8	2
fine & $H/5$	2400000	8, 0.3-9, 8	2.7

quality was also tested with resolved energy criterion.

V. RESULTS

A. Explicit filtering: G1 geometry

The PRS has been filtered to obtain \mathbf{u} , p , the product $\mathbf{u}\mathbf{u}$ and $\boldsymbol{\tau}$. Additionally, the drag term \mathbf{F} was evaluated using the pressure and derivatives of velocity on the boundaries. At first, these operations were done on a smaller filtering domain (depicted in Figure 2 with red lines), to separate the errors related to explicit filtering and the computation of the unclosed terms from the boundary-related commutation errors. The computed fields constitute the results set G1-A. The filter size was set as $\ell_V = 4\sqrt{\pi/6}a$. A comparison of filtered and reference velocity and pressure along the x -axis can be seen in Figure 9. Additionally, the distribution of resolved and filtered velocity fields is visible respectively in Figures 8a and 8b. The distribution of filtered velocity is visibly smeared, however, both filtered fields approach their unfiltered values far away from the obstacle.

The error related to clipping of the filtering molecule manifests itself as inaccurately computed porosity (Figure 8d), which never reaches a value of 1 in the free fluid. The magnitude of \mathbf{F} is presented in Figure 8c. To test the accuracy of the explicit filtering procedure, the residual of the double-averaged momentum equation was computed. Since no filtering near boundaries occurs and $\ell_V = \text{const.}$ all of the commutation error terms are set to 0. The error of the momentum equation is normalised with the maximum imbalance of the stationary equations without the source term, i.e. $\max |(\partial[u_i u_j]/\partial x_j + \partial[\sigma_{ij}]/\partial x_j)|$, and denoted e_{mom} . Its maximal and average values are

presented in Table IV. Since there is no need to evaluate source terms for the continuity equation for this filtering domain, normalised values of continuity errors were not computed.

TABLE IV. Errors resulting from the evaluation of momentum and continuity residuals in all the three cases: G1-A - filtering without commutation errors on the clipped filtering domain, G1-B - filtering with boundary commutation errors, G1-C - inhomogeneous filtering on the small domain.

Case	max e_{mom}	max e_{con}	avg e_{mom}	avg e_{con}
G1-A	0.22%	-	0.019%	-
G1-B	0.23%	0.32%	0.004%	0.034%
G1-C	0.97%	0.86%	0.025%	0.05 %

Both errors related to filtering near the boundary are mathematically the same as the drag force term, so for results set G1-B, they can be evaluated in the same fashion as \mathbf{F} . To capture those errors, filtering has to be conducted in the same domain in which the reference simulation took place. Both \mathbf{F}^b and Λ^b are connected to a decrease of porosity near the edges of the domain (porosity decreases because only part of the kernel overlaps the computational domain). Since the divergence of the product $\phi[\mathbf{u}]$ is the main term in the continuity equation, a decrease in porosity should lead to a forced change of velocity near the boundary. However, since the intrinsic velocity is weighted by the porosity field, it remains similar to the unfiltered distribution, and Λ^b field is required to satisfy the continuity balance.

Distributions of the computed terms are shown in Figures 9a and 9b. The largest values of the sources are located near the inlet and outlet of the domain, consistently with the intuitive

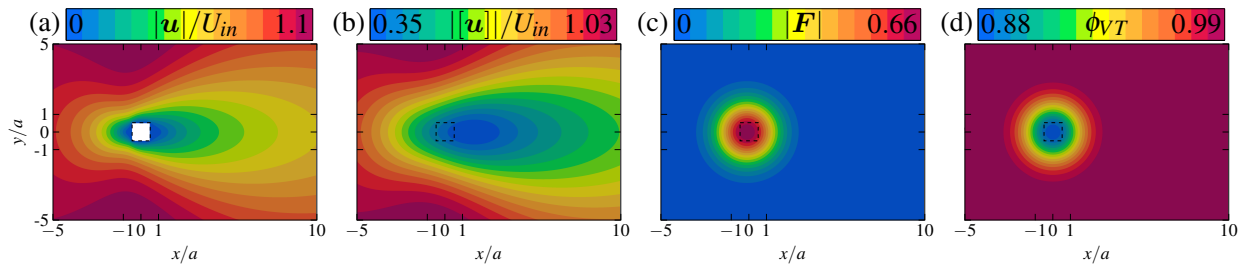


FIG. 7. Distributions of various terms computed from case G1-A, (a) unfiltered velocity field, (b) filtered velocity field, (c) magnitude of computed drag force \mathbf{F} , (d) porosity distribution.

interpretation provided above. The residual of the DANS equations is also evaluated in this study and presented in Table IV. The e_{con} value is the absolute imbalance of the continuity equation normalised by the maximum of $|\partial\phi[u_i]/\partial x_i|$. The errors are comparable to the previous case, signifying a proper resolution of both source terms.

These results also substantiate our observations, related to the possible treatment of non-solid boundaries of the domain in the solver implementing DANS equations, described in Section II A. Since the velocity can be prescribed properly at the inlet (the same boundary condition could be used as for the unfiltered field), there is no reason to assign values of porosity smaller than 1 near non-solid or non-permeable boundaries. Therefore, this decrease in the computed value of porosity can be deemed artificial and such a solver should not require F^b and C^b terms to reproduce explicitly filtered results.

Lastly, the terms F^{ℓ_V} and C^{ℓ_V} were evaluated. The computed set of filtered fields was named G1-C. To isolate them from the influence of boundary-related errors, a smaller domain was used for the filtering. The distribution of ℓ_V was given by the expression $\ell_V = \sqrt{\pi/6}(-3a \arctan(4\sqrt{x_i x_i}/a - 8)/\pi + 5/2a)$. It varies smoothly and reaches a comparable value as in previous tests in the vicinity of the cylinder.

Distributions of both error terms are presented in Figures 9c and 9d. As shown in Appendix D an increased resolution was necessary to ensure proper representation of sharp gradients in the filtered fields. Despite the increase in resolution, the errors (summarised in Table IV) are still

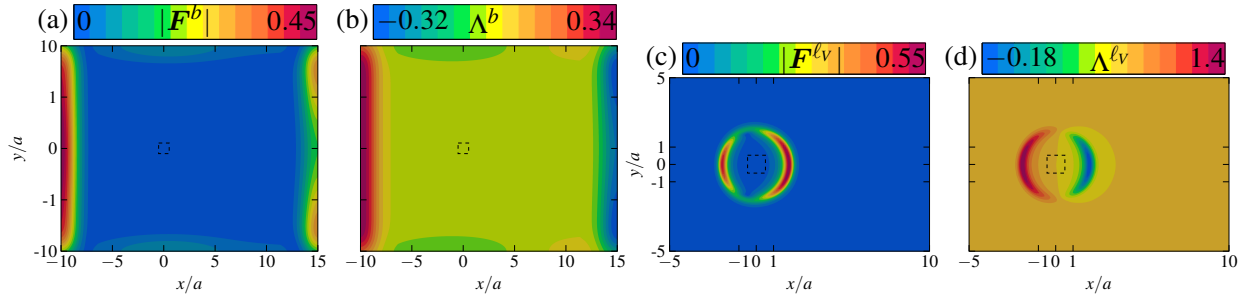


FIG. 8. Distributions of commutation error terms computed from cases G1-B and G1-C, (a) magnitude of boundary error in momentum equation, (b) boundary error in continuum equation (c) magnitude of inhomogeneous spatial filtering error in momentum, (d) inhomogeneous spatial filtering error in continuum equation.

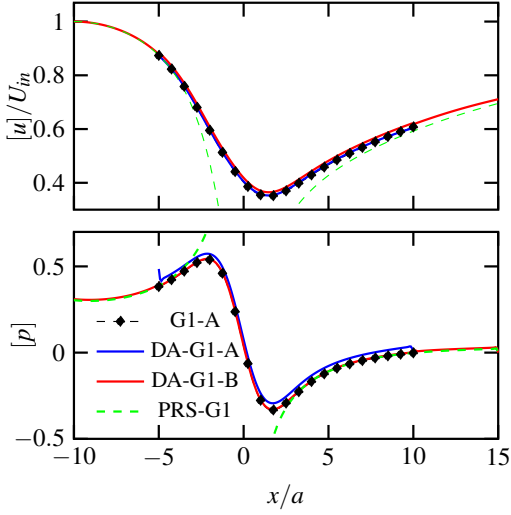


FIG. 9. Plots of the streamwise velocity and pressure: from the particle-resolved simulation, explicitly filtered with a homogeneous filter and results from DANS equations.

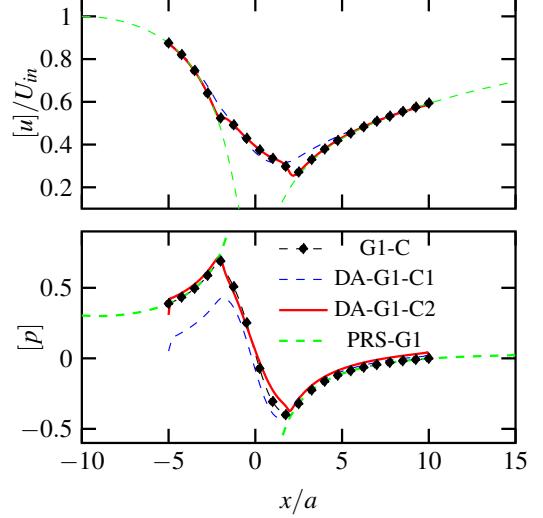


FIG. 10. Plots of the streamwise velocity and pressure: from the particle-resolved simulation, explicitly filtered with an inhomogeneous filter and results from DANS equations assuming accurate or null commutation error in momentum equation.

higher than in the other cases, with the maximum relative momentum error being approximately 1%. Nevertheless, the momentum and continuity errors are small enough to show that all terms were computed correctly in all three cases, thus verifying the derived expressions for commutation errors.

B. Solving DANS equations: case G1

The presented version of the discretised DANS equations was first applied to simulate the flow field from case DA-G1-A. Distributions of the explicitly filtered velocity were used as the boundary conditions in the simulation, for the inlet, upper and lower edges of the domain. For the outlet, a zero gradient boundary condition was employed for velocity along with a reference value for pressure. Residuals of the equations were driven below 10^{-6} to ensure the proper convergence of the nonlinear system. Both the $[u]$ and $[p]$, are in very good agreement with the explicitly filtered data. Plots of both fields along the x -axis are presented in Figure 9. The computed variables are similar to the original fields in areas sufficiently far from the porous region and where both u and p are smooth.

In case DA-G1-B1, F , ϕ and τ fields from G1-A were extrapolated and used for the computation in a domain of the same size as used in the reference simulation. The uniform boundary condition at the inlet and the symmetry conditions at the sides of the domain were prescribed for the filtered velocity. Obtained solution (presented in Figure 9) was in excellent agreement with filtered values. These results support the hypothesis that boundary-related commutation errors need not be included in the computation when the correct porosity is prescribed near the edges of the domain.

Finally, commutation errors connected to the change of ℓ_V were implemented in the solver and tested in case DA-G1-C1. Similarly to the first test, clipped domain and non-uniform Dirichlet conditions were used for velocity. Plots of $[u]$ and $[p]$ are visible in Figure 10. The velocity field is in close agreement with the filtered results. The main feature of the flowfield is the sharp changes of velocity in areas where ℓ_V changes are reproduced very well by the implemented solver. The distribution of intrinsic pressure matches the reference results as well. Additionally, values of $[p]$ near the outlet and inlet are in good agreement with the reference data, aiding in evaluating the pressure drop, one of the important quantities of interest when conducting simulations of packed beds or porous media.

Additionally, the simulation without the commutation errors in the momentum equation was performed. In this case, labelled DA-G1-C2, the filtered velocity fails to account for the changes introduced by the inhomogeneous filtering. Pressure is also reproduced inaccurately. This suggests that including commutation error terms is necessary for the accurate computation of inhomogeneously filtered results in such a simplified configuration. That said, G1-C was computed assuming an arbitrary, fast-changing distribution of ℓ_V . Examination of more realistic flow conditions is necessary to derive more generalisable conclusions.

C. Validation of PRS-G2 case

The quality of the performed LES was estimated using the resolved turbulent kinetic energy criterion. The plot of \overline{M} , including a zoomed view at the region near the top layer of cubes, is visible in Figure 11. The computation on the coarse mesh indicated that the chosen resolution is insufficient, as 80% of the energy was not resolved near the topmost layer of cubes and in the deeper parts of the porous wall. The finer mesh ensures that the criterion of $\overline{M} > 0.8$ is fulfilled in the whole domain. Henceforth, if it is not specified otherwise, we will limit the discussion to the

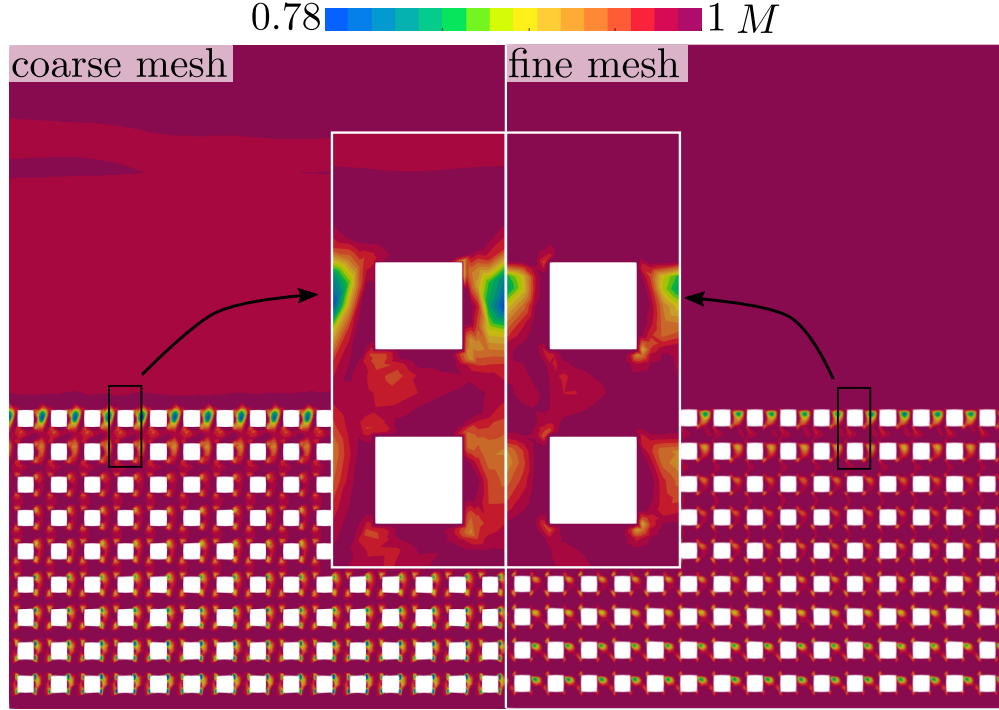


FIG. 11. Time-averaged values of the LES quality criterion, based on resolved turbulent kinetic energy, using the coarse mesh (left) and the fine mesh (right).

results computed on the finer mesh.

The presence of the porous layer at the bottom influences drastically the nature of the flow and turbulence above the cubes. Additionally, the velocity in the porous layer is non-uniform, with the regions of faster fluid penetrating the permeable structure periodically. Such flow is dominated by large-scale, two-dimensional K-H instability^{42,55}, which is probably responsible for the presence of the regions of the faster flow. Figure 12 presents the visualisation of vortical structures with Q criterion contours. The vortices spanning from the porous layer are present in a greater number than typical structures in the boundary layer near the top wall. Additionally, contrary to the elongated structures present in the boundary layer near a smooth boundary, they are not aligned with the streamwise direction, similar to the results reported by Kuwata and Suga⁵⁵.

The results have been filtered with the Cellular kernel assuming $\ell_V = H/10$ (forming result set G2-A1), to facilitate validation and the comparison of our results with the work of Breugem⁴² who used the same filtering molecule. The filter size was constant in the whole domain, apart from the regions near the top and bottom of the domain. There, the kernel was progressively shrunk to ensure that the whole filtering molecule fits in the domain. Following Breugem⁴² we

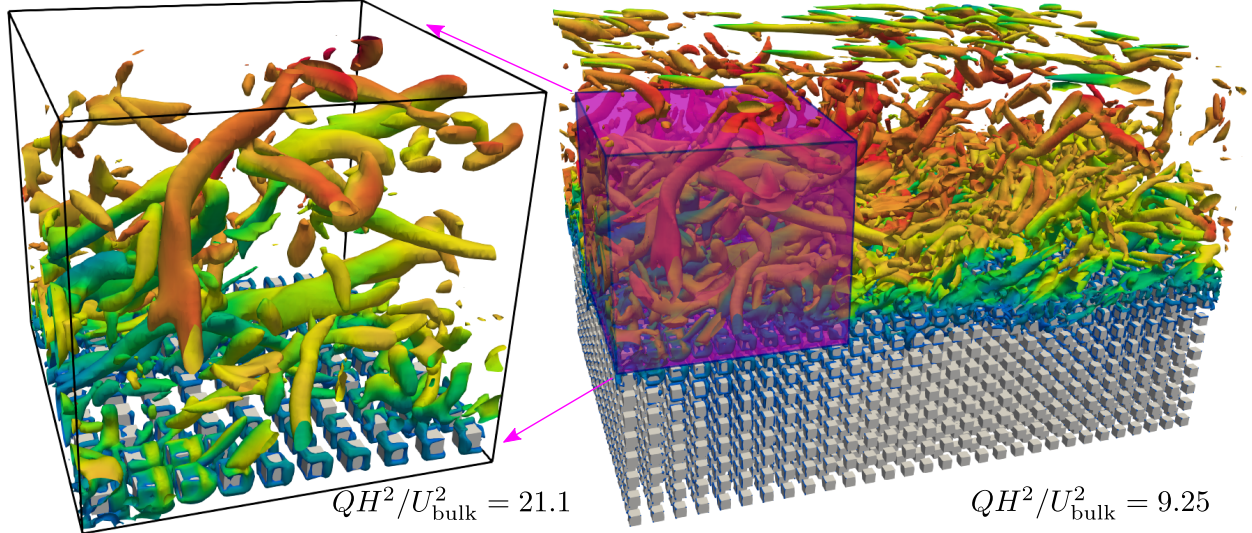


FIG. 12. Q criterion iso-surface colored by the magnitude of velocity.

neglect the resulting commutation error. The accuracy of explicit filtering was once more tested by evaluating the one-dimensional budget of double-averaged momentum. The mean absolute value of imbalance, computed in the region $-0.8 \geq y/H \geq 0.8$ (where $\ell_V = \text{const.}$) was equal to $1.4e-4H/U_{\text{bulk}}^2$ or around 0.6% of the mean pressure gradient driving the flow.

The Reynolds number computed with the top wall friction velocity $Re_{\tau}^t = u_{\tau}^t H / \nu = 393.7$ does not differ greatly from the reported value of 394. The simulation on a coarser mesh resulted in a lower value of $Re_{\tau}^t = 388.2$, even though the resolution near the top wall was sufficient for an accurate reproduction of the boundary layer flow.

The comparison of double-filtered velocity profiles and velocity fluctuations with the reference results is visible in Figure 14. The velocity in the unobstructed part of the channel is predicted correctly on both meshes, while the coarser grid underpredicts the velocity in the porous part of the domain. Additionally, on the coarser mesh, the velocity reaches the uniform value closer to the topmost layer of cubes. The streamwise and wall-normal fluctuations are predicted accurately on the fine mesh and underestimated in the porous region on the coarser mesh.

Contrary to the rest of the profiles, the distributions of the spanwise fluctuations differ greatly between the two meshes. The fine mesh reproduces the DNS results well. The coarse LES underestimates the fluctuations in both boundary layers, while overpredicting spanwise motions inside the porous layer. Worse results on the coarse mesh can naturally be attributed to greater cell spacing. However, on both meshes, the cell sizes were identical in x and z directions, which intuitively

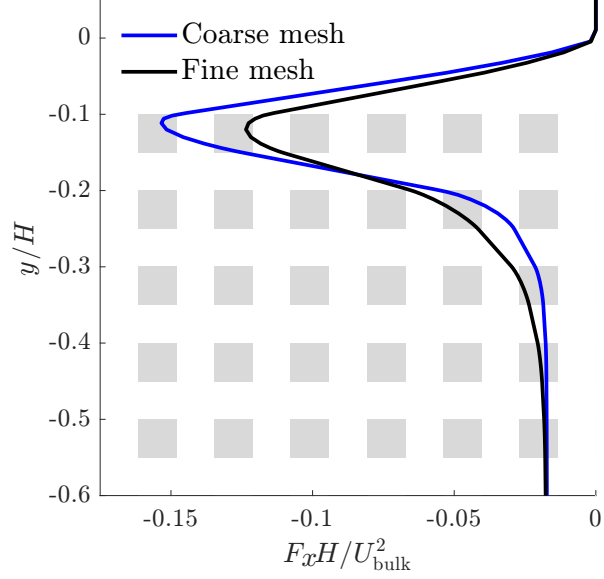


FIG. 13. The drag force experienced by the fluid on the two meshes used in the PRS-G2 simulation.

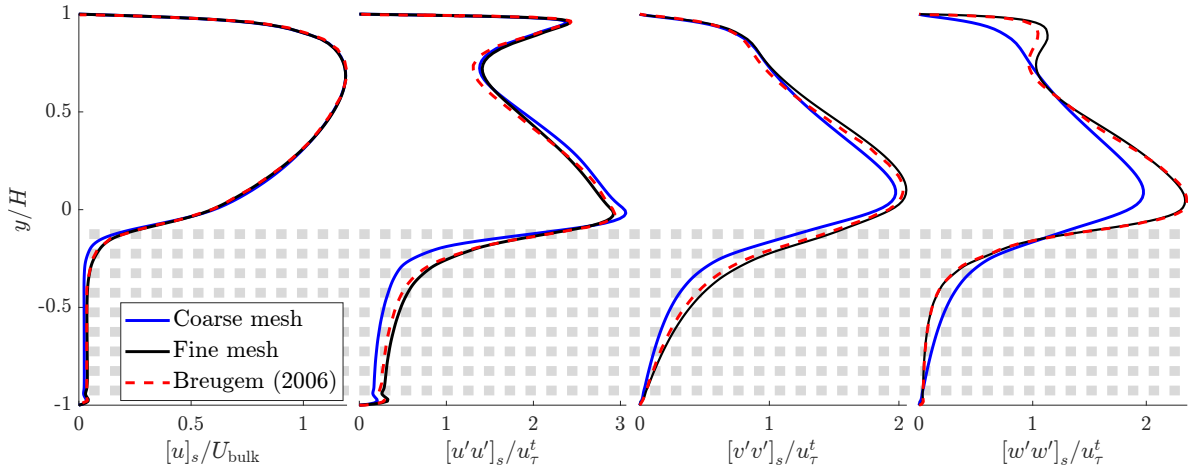


FIG. 14. Filtered results from PRS-G2 case computed on the coarse and fine mesh ($\ell_V = H/10$), compared to the reference DNS⁴².

should result in a similar accuracy of the prediction of the streamwise and spanwise velocity fluctuations.

An alternative explanation for the inaccurately computed spanwise fluctuations on the coarse mesh might relate to the presence of the K-H instability. When the resolution near the top layer of cubes is insufficient, the transfer of energy from the large-scale vortices in the free flow to the fluid inside the porous region will not be reproduced accurately. The generation of the spanwise motions

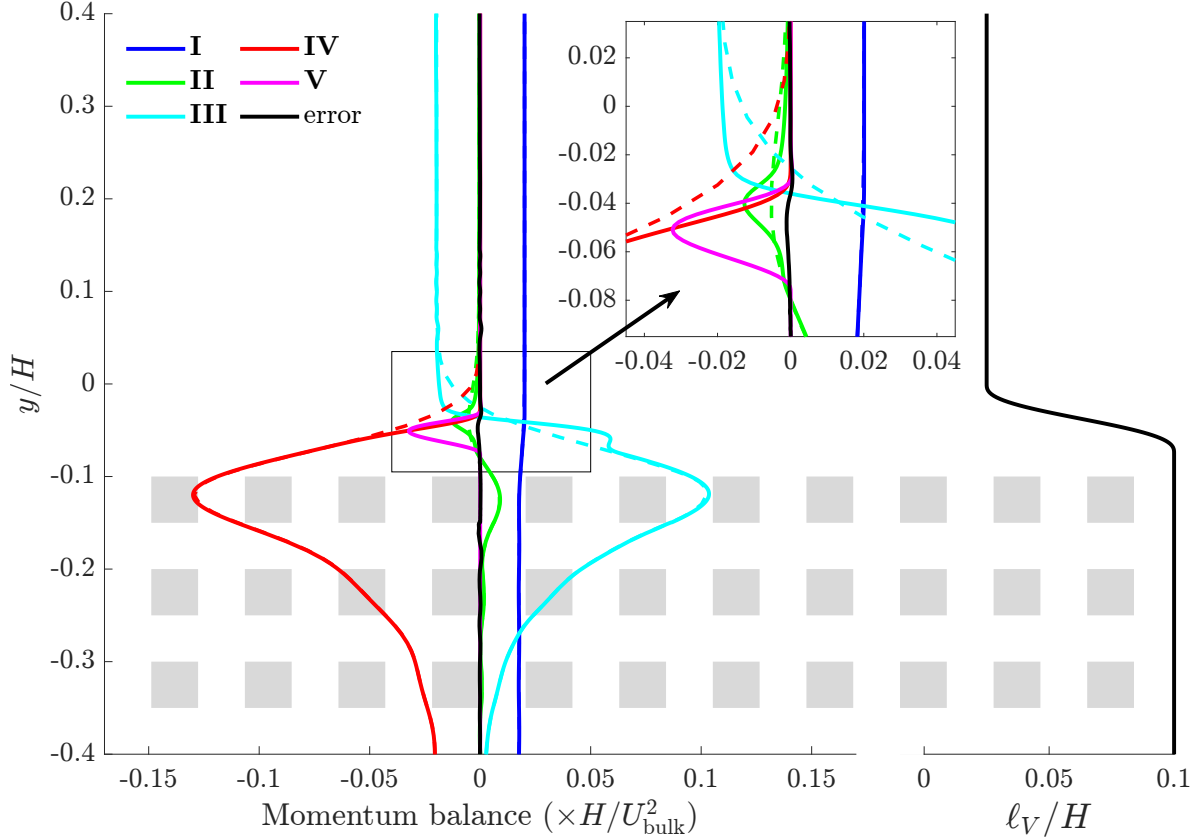


FIG. 15. **Left:** space-time filtered momentum balance in the middle of the channel. Solid lines describe the terms defined in Eq. (42), evaluated with Gaussian kernel assuming changing filtering width. Their counterparts evaluated with the same kernel assuming $\ell_V = H/10$ are displayed with dashed lines. **Right:** distribution of filter size.

in the boundary layers will depend on the breakdown of wall-normal and streamwise fluctuations and is also connected to the accuracy with which the two-dimensional K-H instability is resolved. Therefore, insufficient resolution in the porous layer will lead to a less accurate prediction of spanwise fluctuation in the clear channel.

Nevertheless, the fine mesh allows for sufficiently accurate LES simulation resolving both first- and second-order statistics with good accuracy. The last important parameter that needs to be compared between meshes is the predicted drag force distribution. Drag forces computed from explicit filtering are visible in Figure 13. Since the simulation on the fine mesh results in a correct value of Re_τ^t and properly predicted mean profiles, we will consider the distribution of the drag force from this simulation as an accurate reference. In comparison, coarser mesh overpredicts

the drag force near the topmost layer of cubes which is a direct result of increased numerical dissipation resulting from not sufficient resolution. It provides evidence, that a slight change in resolution and gridding methodology can influence greatly the drag force distribution and by extent the mean velocity in the porous region. Therefore, the process of generating a grid for a particle-resolved LES should be done with great care.

D. Commutation errors at the porous-fluid interface

The particle-resolved simulation has been also used to evaluate the commutation errors in the momentum equation. For this part of the study Gaussian function was used as a kernel instead of Cellular weighting function. As pointed out by^{41,42} and our previous work⁴⁰, Cellular kernel is better suited to such geometry at a chosen filter size of $\ell_V = H/10$. However, computation of commutation errors requires the evaluation of the kernel derivative w.r.t. ℓ_V , which would be discontinuous in the case of Cellular kernel and introduce additional errors into the investigation. Additionally, owing to the scaling ensured by Eq. (21), filtering with Gaussian kernel provides similar distributions of filtered fields.

We confine this analysis to the commutation error of the divergence and stress tensor terms, which together give the \mathbf{F}^{ℓ_V} source term. We omit the commutation errors related to the derivatives present inside the stress tensor, as is difficult to ensure that they are computed accurately, due to non-constant viscosity in the LES equations. We also do not consider the terms in the continuity equation, as the flow is assumed to be statistically one-dimensional, which in turn necessitates a zero source term in the continuity equation.

While performing a DNS combined with VANS equations, Breugem⁴² assumed that the filter changes in the region where porosity increases from 0.875 to 1, that is for $0.075H < y < 0$. To investigate the magnitude of those errors we prescribe the distribution of ℓ_V using Equation (41), assuming that $(\delta^-, \delta^+) = (0.075H, 0)$. The filter size changes from $H/10$ inside the porous region to the value of $H/40 \approx 9.8^{+t}$, which is comparable to the resolution in the centre of the channel, offered by the fine mesh used for particle-resolved LES. The resultant ℓ_V curve is visible in Figure 15.

The momentum budget in the streamwise direction including the commutation error can be

given as

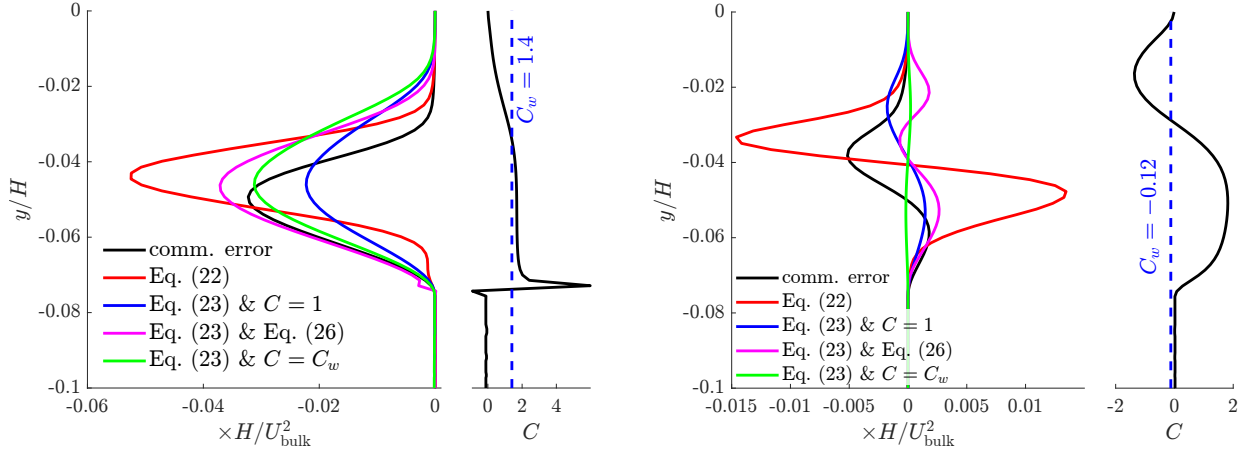
$$\begin{aligned}
0 = & \underbrace{-\phi \frac{\partial [p]}{\partial x}}_{\text{I}} + \underbrace{\frac{\partial}{\partial y} \left[\nu_{\text{eff}} \left(\frac{\partial u}{\partial y} + \frac{\partial v}{\partial x} \right) \right]_s}_{\text{II}} + \underbrace{\frac{\partial \phi ([u][v] - [uv])}{\partial y}}_{\text{III}} + \underbrace{F_x}_{\text{IV}} \\
& + \underbrace{\frac{\partial \ell_V}{\partial y} \left\{ \frac{\partial G}{\partial \ell_V} \star \left(\gamma_{uv} - \gamma \nu_{\text{eff}} \left(\frac{\partial u}{\partial y} + \frac{\partial v}{\partial x} \right) \right) \right\}}_{\text{V}}, \tag{42}
\end{aligned}$$

with the terms **I-V** denoting effective pressure gradient, the contribution of viscous and sub-filter stresses, drag force and commutation error respectively. The commutation error related to the pressure gradient is equal to zero, as the gradient of ℓ_V is aligned with the wall-normal direction.

The accuracy of the computation of the commutation error is tested by evaluating Equation (42). The distribution of the terms is shown in Figure 15 along with the curves computed with the constant filter size. Non-uniform filtering width introduces an error by changing the contributions of different terms to the momentum balance. Decreasing filter size leads to a faster change of the drag force and an abrupt change of the derivative of the viscous and sub-filter stresses. This behaviour adds validity to the discontinuous method of modelling the interface, where the stress jump is prescribed at the coupling porous-fluid boundary (see e.g.⁵⁶ for this method applied to the channel flow). In such an approach the filtering size is different on both sides of the boundary. Assuming that ℓ_V changes continuously over such an interface, albeit with a steep gradient, it has to result in a commutation error and an abrupt change in the stresses. Therefore, imposing a stress jump at this location can be seen as a method to account for some part of the commutation error.

When included in the momentum budget, the commutation error acts as a sink effectively increasing drag in the region where filtering width changes. Locally, its contribution is significant as it is comparable to drag. However, it only constitutes 2.5% of the total combined source term in the momentum equation, in the $-0.8 \geq y/H \geq 0.8$ region.

The commutation error arising from filtering $\partial u_i u_j / \partial x_j$ constitutes the main contribution to $F_x^{\ell_V}$ (Figure 16a). The value obtained from the particle-resolved simulation has been compared to the models presented in Section III B. Equation (29) does not provide a good prediction of the error distribution. On the other hand, an approach based on the scale-similarity hypothesis provides a much better estimation of the commutation error. If the coefficient in Equation (30) is chosen as $C = 1$, the model is relatively inaccurate, however, if the distribution of C is determined according to Equation (33), it performs much better, especially for the lower portion of the region in which



(a) commutation error related to the convection term,

given by $(\partial\ell_V/\partial x_i)(\partial G/\partial\ell_V) \star (\gamma u_i u_j)$

(b) commutation error related to the convection term,

given by

$$(\partial\ell_V/\partial x_i)(\partial G/\partial\ell_V) \star (-\gamma_{\text{eff}}(\partial u_i/\partial x_j + \partial u_j/\partial x_i))$$

FIG. 16. Commutation errors assuming distribution of filter size drawn in Figure 15. It is compared to an approximation of the CE given by Equations (29) and the scale-similarity model. Three different methods for specifying the model coefficient are presented. The distribution of the coefficient C computed from Eq. (33) along with the value of its average weighed by $|\partial\ell_V/\partial x_i|$ (blue dash line) are visible on the right.

filter changes size. That being said, the value of C changes drastically around $y = -0.075H$. In the world of dynamic LES models, such behaviour is usually remedied by averaging the coefficient in homogeneous directions¹. Following this method, C was determined by averaging the values obtained from Eq. (33) with the absolute value of $\partial\ell_V/\partial y$ as a weight:

$$C_w = \int_{-H}^H C \left| \frac{\partial\ell_V}{\partial y} \right| dy \left(\int_{-H}^H \left| \frac{\partial\ell_V}{\partial y} \right| dy \right)^{-1}. \quad (43)$$

This resulted in a value of $C_w = 1.4$. the model with $C = C_w$ has the best overall performance, reproducing accurately the values of the error for the lower portion of the interface while limiting the overprediction for higher y coordinates.

The error related to the divergence of the stress tensor (Figure 16b) constitutes a much smaller part of the overall commutation error. This is an expected result, as the sub-filter stresses and drag force have the most substantial contributions to the momentum budget. Each of the tested models was not able to predict the distribution of the error with sufficient accuracy. The bad performance of the scale-similarity model stems from the computed distribution of C , which changes the sign in the middle of the interface region. This also results in a near zero value of the weighted average

C_w . The bad performance of both methods for this particular term is discouraging, however, since the commutation error related to the viscous term has little impact on the momentum balance, it can be safely neglected while the modelling of CEs is attempted, without impeding the accuracy of results.

E. Solving DANS equations: case G2

The solutions obtained on the coarse meshes did not deviate much from the ones computed on the finer ones. Each of the simulations resolved more than 95 % of turbulent kinetic energy locally, therefore the resolution of the coarser mesh can be deemed sufficient for such simulations. In the following section, the results from the finer meshes will be presented.

Considering that an *a-posteriori* analysis of the commutation error performed in Section VD indicated that the CE does not have a detrimental effect on the momentum balance, it was neglected in DA-G2 simulations. As in the case of Breugem⁴², who performed a DNS, a good correspondence between the solution of modelled equations and the results of PRS can be observed. Focusing first on results of DA-G2-A1 (assuming $\ell_V = H/10$ the profile of mean velocity in the clear section of the channel (Figure 17) is slightly shifted towards the upper wall. The mean velocity in the porous and interface regions is also predicted with sufficient accuracy. Figure 17 also presents resolved normal fluctuations computed in all directions. Due to the fact that time and spatial filtering can be applied in an interchangeable order, the double-averaged fluctuation can be computed as $\langle u'_i \rangle = \overline{\langle u_i \rangle} - \langle u_i \rangle$. This results in the following definition of the components of double-averaged resolved fluctuations:

$$[u'_i u'_j]_s = \phi \overline{\langle u'_i \rangle \langle u'_j \rangle} + \phi \left(\overline{\langle u'_i u'_j \rangle} - \overline{\langle u'_i \rangle \langle u'_j \rangle} \right) \quad (44)$$

The term enclosed in parenthesis on the right-hand-side cannot be directly computed from the solution of filtered equations, therefore, it has to be neglected.

The components of the resolved TKE are consistently underestimated in the porous part of the domain. On the other hand, they are accurately predicted near the top wall, in the boundary layer. The fluctuations near the topmost layer of cubes are also computed with reasonable accuracy. All of the above suggests, that the chosen drag closure is a viable method to be used with an LES model. Obtained solutions offer similar fidelity as the reference DNS⁴².

The increase of assumed filter size leads to the change of the explicitly filtered velocity profile at the interface, with the higher velocities penetrating the porous structure deeper. This change is

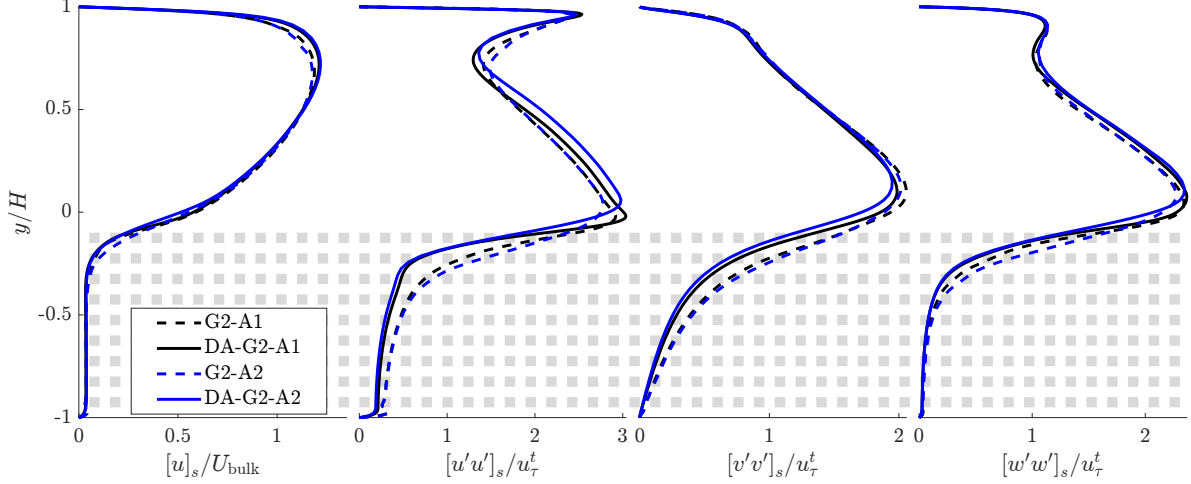


FIG. 17. Comparison of the profiles from the double-averaged particle-resolved LES and LES with DANS equations results averaged in time. The results are presented for two different filter sizes, for G2-A1 case $\ell_V = H/10$ and for G2-A2 $\ell_V = H/5$.

not reproduced in the results obtained with the implemented solver. The velocity profile is only slightly affected by the change in filter size. However, it does have an effect on the second-order statistics, as the increase of ℓ_V shifts the peak of resolved fluctuations in the lower boundary layer upwards.

The profiles of drag force around the interface region are presented in Figure 18. For both filter sizes, the magnitude of the force is overestimated. In fact, comparing total drag force from explicitly filtered PRSs and the drag model $F_x = -\nu \mathcal{K}^{-1} (1 + \mathcal{F}) \phi^2 [u]$, the simulation assuming $\ell_V = H/10$ predicts 1.1 greater drag. The accuracy of the model seems to decrease with increasing filter size, as for $\ell_V = H/5$, this ratio is equal to 1.21. In the model, the force is proportional to the predicted velocity. For $\ell_V = H/10$ the model resembles the shape of the drag curve obtained from the PRS much more closely, which results in a slightly more accurate velocity prediction. In both cases, the magnitude of the drag force curve rises in a similar fashion while approaching the interface from below, which explains why both filter sizes ultimately result in similar velocity distributions in this region.

The change in the porosity at the interface has a limited effect on the overall performance of the model. However, if the flow near the porous-fluid interface is to be investigated, then the profile of ϕ has to be selected carefully. For example, if Darcy–Forcheimer closure is chosen then ϕ might be determined in such a way that generates the best approximation of \mathbf{F} at the interface. This

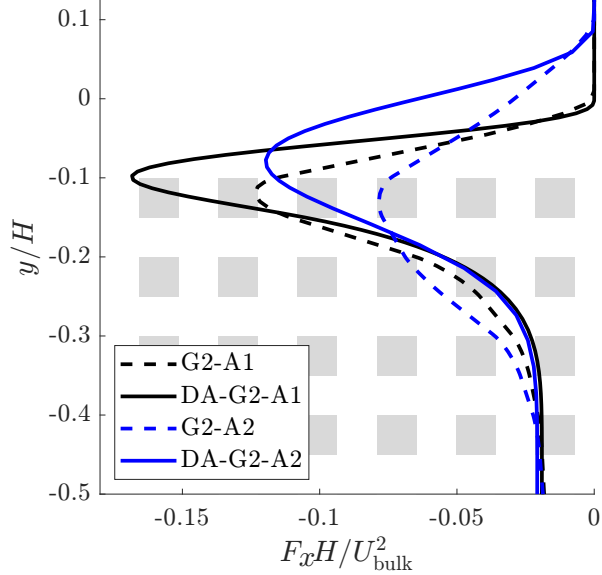


FIG. 18. Comparison of the drag force from the filtered PRSs and LES done with the DANS solver. The results are presented for two different filter sizes, $\ell_V = H/10$ and $H/5$.

can naturally only be achieved if the results of a more accurate, particle-resolved simulation are available. Ultimately, as also pointed out by Sadowski and di Mare⁴⁰, the fact that the change of ℓ_V has an influence on the accuracy of drag force computation indicates that the closure should include the influence of that parameter, either by correcting \mathcal{H} and \mathcal{F} or other means.

VI. CONCLUDING REMARKS

In the present study, the mathematical foundations of the double-averaging framework for flows in porous media have been rigorously reformulated as filtering with a space-time kernel. The averaging theorems used extensively in the derivation of Double-Averaged Navier Stokes equations have been generalised to work with any well-behaved kernel functions and extended to include commutation errors of filtering/derivative operators.

This development lays the groundwork for using DANS equations with inhomogeneous filtering, an important property of the equations for flow configurations where significant changes in the pore or particle size occur. Additionally, relationships describing the errors arising when filtering next to a boundary are derived and included in the equations. These errors have fundamentally the same form as boundary integrals forming the unclosed drag force terms.

The newly derived equations are tested by explicitly filtering a simplified particle-resolved simulation with a Gaussian filter and evaluating the residual of both momentum and mass conservation. Although only spatial filtering has been conducted, this has proved sufficient to verify the derivation of mathematical description of the errors. The largest relative momentum error (around 1%) has been found in the inhomogeneous filtering case, suggesting that extensive analysis of grid requirements for a given distribution of filter width might be necessary.

Furthermore, the particle-resolved LES of the fully developed turbulent flow in a channel partly occupied by a porous structure has been realised. The computation has been performed on two meshes, testing the grid requirements for an accurate scale-resolving simulation in such a setting. Insufficient resolution near the surface of the porous wall led to inaccurately predicted mean velocity in the whole porous region of the channel and greatly overestimated porous-induced drag force, even though, the results in the unobstructed region agree qualitatively with the reference DNS.

The results from the LES have also been explicitly filtered. The assumed distribution of the kernel molecule was non-uniform, transitioning from a size adequate to homogenise the porous medium to a smaller filter in the unobstructed region, representing the filtering requirements for an LES. Resulting commutation error have been computed and compared to other terms contributing to the momentum balance. In such a configuration, the error acts as an additional sink term in the momentum equation, effectively increasing the drag force, albeit by a small margin, as it only constituted around 2.5% of the total effective drag.

The bulk of the commutation error is related to the derivative of the convective term in the Navier-Stokes equations. The error manifests itself as a decrease in the magnitude of the drag force and a local abrupt change in the divergence of the sub-filter and viscous stresses. This behaviour adds validity to the discontinuous treatment of the porous-fluid interface with the stress jump boundary conditions. Such coupling can be viewed as a method of modelling the commutation error arising from a discontinuous change in the filter size.

Two different approaches for modelling the commutation error have been investigated, based on the differential approximation of the filtering operation and the scale-similarity hypothesis. The first one, while easier to implement did not yield good results. The latter, when the model constant has been averaged, was able to qualitatively reproduce the error related to the convective term.

A solver for double-filtered equations, based on the PIMPLE algorithm has been implemented in OpenFOAM. The numerical scheme can reproduce the explicitly filtered results with very good

accuracy, employing source terms gathered from explicit filtering. Additionally, the significance of the error source terms has been investigated for the accurate computation of filtered velocity and pressure. This analysis revealed that the inclusion of boundary commutation errors is not necessary in both the momentum and continuity equation when the porosity distribution is properly prescribed in those areas.

Finally, the channel flow has also been simulated with a combined LES porous-medium model, which assumed eddy-viscosity closure in the whole domain. The porosity was prescribed to resemble the profile obtained from the explicitly filtered results, considering two different filter sizes. Following the conclusions, that commutation errors might not have a critical impact on the results in such configuration, they have been neglected. The solution was found to be in good agreement with explicitly filtered particle-resolved LES results. However, computed fields did not reflect the rather subtle changes of filtered quantities at the interface, occurring with an increase in filter size. This seems to be a result of the inaccuracy of the drag closure which overpredicted the total drag by 10% for the smaller of the chosen filter sizes and 20% for the larger one.

The presented mathematical framework opens doors to several possibilities for future research. First and foremost a full-scale flow configuration e.g. gaseous flow in a lime kiln could be evaluated using explicit filtering. The forces, dispersion stresses, turbulent quantities and filtered scalar fluxes could be compared to the currently employed models. Even though the investigated numerical method resulted in a qualitatively accurate prediction of the flow at the fluid-porous interface, it is important to stress that the drag closure was tuned to the present geometrical configuration (i.e. array of cubes). Therefore, gathering more data from particle-resolved simulations should aid in the derivation of a more general approach for drag modelling. Additionally, the investigation of the drag closure seems like a more promising avenue to increase the fidelity of the simulation of porous-fluid systems, as it contributes the biggest error to the momentum balance.

CONFLICT OF INTEREST

The authors have no conflicts to disclose.

AUTHOR'S CONTRIBUTIONS

Wojciech Sadowski: conceptualization (equal), data curation, formal analysis (lead), writing/original draft preparation (lead), methodology, software, validation (lead), visualization (lead), writing/review & editing (equal). **Mohammed Sayyari:** formal analysis (supporting), validation (supporting), visualisation (supporting), writing/original draft preparation (supporting), writing/review & editing (equal). **Francesca di Mare:** conceptualization (equal), formal analysis (supporting), funding acquisition, project administration, supervision (lead), writing/review & editing (equal). **Holger Marschall:** conceptualization (equal), writing/review & editing (equal), writing/original draft preparation (supporting).

ACKNOWLEDGEMENT

The authors gratefully acknowledge financial support from the Deutsche Forschungsgemeinschaft (DFG) through SFB/TRR287, Project Number 422037413. The authors also wish to thank Dr. Pascal Post for the fruitful discussions and suggestions given during preparation of this manuscript.

Appendix A: The superficial space-time averaging technique

The superficial space-time average²⁹ of variable $\psi(\mathbf{x}, t)$, denoted as $[\psi]_s$, is defined as

$$[\psi]_s(\mathbf{x}, t) = \frac{1}{T_0 V_0} \int_{T_0 \times V_0} \psi(\mathbf{x} + \boldsymbol{\xi}, t + \tau) \gamma(\mathbf{x} + \boldsymbol{\xi}, t + \tau) d\boldsymbol{\xi} d\tau. \quad (\text{A1})$$

The function γ is often called a clipping or phase indicator function^{29,39}. It describes the distribution of the fluid phase in space and time,

$$\gamma(\mathbf{x}, t) = \begin{cases} 1, & \text{if the particle at } \mathbf{x}, t \text{ is fluid;} \\ 0, & \text{otherwise.} \end{cases} \quad (\text{A2})$$

The superficial average and the space-time porosity ϕ_{VT} are related by the formula for the intrinsic average denoted with $[\cdot]$

$$[\psi]_s = \phi_{VT}[\psi], \quad (\text{A3})$$

where the space-time porosity is defined as

$$\phi_{VT} = [1]_s = \frac{1}{T_0 V_0} \int_{T_0 \times V_0} \gamma(\mathbf{x} + \boldsymbol{\xi}, t + \tau) d\boldsymbol{\xi} d\tau. \quad (\text{A4})$$

To obtain a space-time averaged system of differential equations, the superficial averages are applied to the time and space partial derivatives respectively. Next the averaging theorems are used to introduce the averaging operators under the derivatives. Initial derivations of these theorems for VANS with the discussion of their properties can be found in works by Whitaker⁵⁷ and Howes and Whitaker⁵⁸. Gray and Lee⁵⁹ followed a different approach to prove both theorems, using the phase indicator function γ and its derivatives⁶⁰, which was later extended by Nikora *et al.*^{28,29} to obtain the relations presented above. The main assumption in each proof is that *the averaging volume remains space-invariant*. The theorems describe the relationship between the average of the derivative and the derivative of the average in the following way:

$$\left[\frac{\partial \psi}{\partial t} \right]_s = \frac{\partial [\psi]_s}{\partial t} + \frac{1}{V_0} \overline{\oint_S \psi w_i n_i dS}^s, \quad (\text{A5})$$

$$\left[\frac{\partial \psi}{\partial x_i} \right]_s = \frac{\partial [\psi]_s}{\partial x_i} - \frac{1}{V_0} \overline{\oint_S \psi n_i dS}^s. \quad (\text{A6})$$

S is the interface region between the fluid and solid phases inside averaging volume V_0 , \mathbf{n} is the inward normal vector of the fluid region and \mathbf{w} is the velocity of the interface. Overbar with subscript s denotes superficial time average. Using equation (2), both theorems can be used with intrinsic quantities.

Appendix B: Derivation of DANS equations

We start by averaging the system (8) in space and time following Nikora *et al.*²⁹. Using Equations (A5) and (A6) results in the following momentum equation:

$$\rho \left(\frac{\partial [u_i]_s}{\partial t} + \frac{\partial [u_i u_j]_s}{\partial x_j} \right) = \frac{\partial [\sigma_{ij}]_s}{\partial x_j} + \rho [f_i]_s + \rho F_i, \quad (\text{B1})$$

where \mathbf{F} represents the interfacial forces introduced with surface integrals while applying averaging theorems:

$$F_i = -\frac{1}{V_0} \overline{\oint_S \sigma_{ij} n_j dS}^s. \quad (\text{B2})$$

Equation (B1) is an intermediate step for obtaining DANS momentum equation. The next step requires changing the averages into their intrinsic counterparts. The choice of writing the equation with intrinsic averaging has two advantages. First, as shown by²³, intrinsic averaging preserves constants, where superficial averaging does not. Second, the intrinsic average results in a proper decomposition of the convection term. The dispersion terms resulting from performing such decomposition assuming superficial average cannot be modelled by a diffusion-like mechanism³¹. In both cases, an improper choice of the averaging type may result in an error that is of the order of magnitude of the porosity. Additionally, inconsistent formulation of the DANS system with superficial variables may lead to non-Galilean invariant set of equations⁶¹. We will employ intrinsic averages in the course of this work, however, it is important to note that, if used with care, superficial variables can be used with success and accuracy^{42,56}.

Rewriting Equation (B1) using the intrinsic average results in

$$\rho \left(\frac{\partial \phi_{VT}[u_i]}{\partial t} + \frac{\partial \phi_{VT}[u_i u_j]}{\partial x_j} \right) = \frac{\partial \phi_{VT}[\sigma_{ij}]}{\partial x_j} + \rho \phi_{VT}[f_i] + \rho F_i. \quad (\text{B3})$$

In the second term in the left-hand side of Equation (B3), the average of the product of velocities must be decomposed:

$$[u_i u_j] = [u_i][u_j] - \tau_{ij} = [u_i][u_j] - ([u_i][u_j] - [u_i u_j]), \quad (\text{B4})$$

where τ represents porous dispersion and must be modeled, if its influence on the behaviour of the flow is to be included in the mathematical derivation. However, it is often the case that this term is neglected in the final equations (analysis of the significance of τ in the context of VANS framework can be found in works of Breugem, Boersma, and Uittenbogaard³⁹). The averaged continuity equation is derived in a similar fashion. The result is that the space-time averaged Navier-Stokes equations:

$$\frac{\partial \phi_{VT}}{\partial t} + \frac{\partial \phi_{VT}[u_i]}{\partial x_i} = 0, \quad (\text{B5a})$$

$$\rho \left(\frac{\partial \phi_{VT}[u_i]}{\partial t} + \frac{\partial \phi_{VT}[u_i][u_j]}{\partial x_j} \right) = \frac{\partial \phi_{VT}[\sigma_{ij}]}{\partial x_j} + \frac{\partial \rho \phi_{VT} \tau_{ij}}{\partial x_j} + \rho \phi_{VT}[f_i] + \rho F_i, \quad (\text{B5b})$$

Appendix C: Derivatives for evaluation of commutation errors

This section outlines formulas for derivatives, necessary for simplification of equation for the commutation error of space-time filter. First, the derivative of a filter kernel is given by (s is a

placeholder for x_i or t)

$$\frac{\partial G(\boldsymbol{\xi}, \tau, \ell_V(\mathbf{x}), T_0(t))}{\partial s} = \frac{\partial G}{\partial \xi_i} \frac{\partial \xi_i}{\partial s} + \frac{\partial G}{\partial \tau} \frac{\partial \tau}{\partial s} + \frac{\partial G}{\partial \ell_V} \frac{\partial \ell_V}{\partial x_i} \frac{\partial x_i}{\partial s} + \frac{\partial G}{\partial T_0} \frac{\partial T_0}{\partial t} \frac{\partial t}{\partial s}, \quad (\text{C1})$$

which leads to following simplifications under the assumptions made in section II A:

$$\frac{\partial G(\boldsymbol{\xi}, \tau, \ell_V(\mathbf{x}), T_0(t))}{\partial x_i} = \frac{\partial G}{\partial \ell_V} \frac{\partial \ell_V}{\partial x_i}, \quad (\text{C2a})$$

$$\frac{\partial G(\boldsymbol{\xi}, \tau, \ell_V(\mathbf{x}), T_0(t))}{\partial t} = \frac{\partial G}{\partial T_0} \frac{\partial T_0}{\partial t} \quad (\text{C2b})$$

The spatial derivative of the clipping function^{58,59} can be defined as

$$\frac{\partial \gamma}{\partial x_i} = n_i \delta(\mathbf{x} - \mathbf{x}_S), \quad (\text{C3})$$

where δ is the Dirac function, \mathbf{x}_S is a vector “tracing” the interface S and \mathbf{n} is a normal vector defined as in section II A. The time derivative of γ can be found after noticing that the material derivative of γ is zero for an observer sitting on the iso-surface (respectively iso-line) of $\gamma = 1$ (i.e. where $\mathbf{x} = \mathbf{x}_S$). Owing to that

$$\frac{\partial \gamma}{\partial t} = -w_i \frac{\partial \gamma}{\partial x_i} = w_i n_i \delta(\mathbf{x} - \mathbf{x}_S), \quad (\text{C4})$$

where \mathbf{w} is the velocity of the interface. For completeness, the derivatives of the shifted functions under the convolution integral can be obtained in the following manner:

$$\frac{\partial f(\mathbf{x} - \boldsymbol{\xi}, t - \tau)}{\partial s} = \frac{\partial f}{\partial (x_i - \xi_i)} \frac{\partial (x_i - \xi_i)}{\partial s} + \frac{\partial f}{\partial (t - \tau)} \frac{\partial (t - \tau)}{\partial s}, \quad (\text{C5})$$

leading to:

$$\frac{\partial f(\mathbf{x} - \boldsymbol{\xi}, t - \tau)}{\partial x_i} = \frac{\partial f}{\partial (x_i - \xi_i)}, \quad (\text{C6a})$$

$$\frac{\partial f(\mathbf{x} - \boldsymbol{\xi}, t - \tau)}{\partial t} = \frac{\partial f}{\partial (t - \tau)} \quad (\text{C6b})$$

Appendix D: Sensitivity study of explicit filtering w.r.t. kernel clip distance d and filtering mesh resolution

Explicit filtering method, as described in⁴⁰, can have multiple sources of errors, that have to be considered and controlled while analysing filtered quantities. Firstly, if the mesh is too coarse to accurately represent the chosen filter, this can introduce an error due to insufficient resolution of

numerical integration. Secondly, if the spatial resolution differs greatly between the two parts of the domain, the difference in accuracy of convolution computation will introduce oscillations in the filtered fields.

Moreover, as described in the section III the filter kernel is being clipped to 0 after a certain distance d from the center of the filtering molecule. This can introduce additional significant error to the filtering operation. A clipped kernel, which originally had an infinite support, does not conserve constants, which also means that the filtered flow will be wrongly represented.

All of those inaccuracies will accumulate and influence the momentum balance. For example, oscillations in porosity field resulting from the errors, will be carried over to other quantities of interest and increased by the use discrete derivative operators, e.g. when evaluating $\text{div}(\phi[\mathbf{u}][\mathbf{u}])$.

To test what value of d is required for accurate representation of the filter, a sensitivity study was performed with a set of distances $d/\ell_V = \{0.8, 1, 1.2, 1.5, 1.8\}$ using both cases G1-A and G1-C. The corresponding filter shapes (the Gaussian filter and its derivative with respect to filter width ℓ_V) are drawn on Figures 19a and 19b in their one-dimensional forms. The shapes of the both kernels alone, suggest that latter will require greater value of d/ℓ_V to ensure proper resolution.

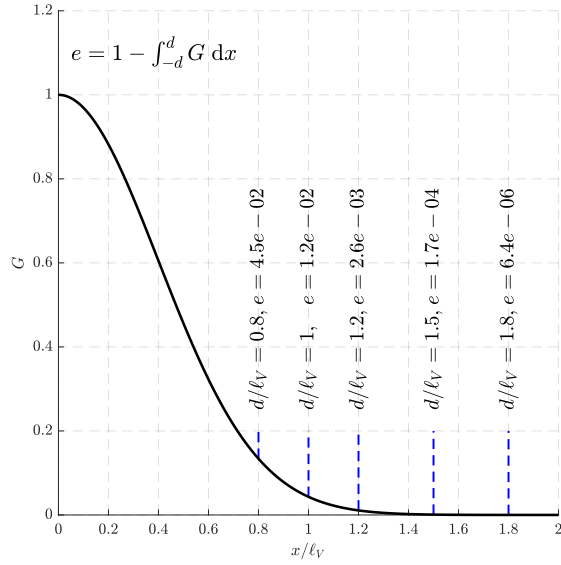
For each value of d/ℓ_V the cases were filtered and residuals of double-filtered equations were evaluated as described in section V. Obtained error values are plotted in the figures 20a and 20b. Inspection of the errors from case G1-A reveals that increasing the clipping distance beyond $d/\ell_V = 1.2$ does not decrease the evaluated residuals, therefore this value has been selected as a minimal clipping distance for filtering with Gaussian filter.

Based on the results from case G1-C, the minimal clipping distance for the derivative was chosen to be $d/\ell_V = 1.5$. Since the values of the computed residuals did not decrease to values similar to case A, filtering mesh (the mesh used for evaluation of balance of filtered quantities) sensitivity study was additionally performed for case G1-C.

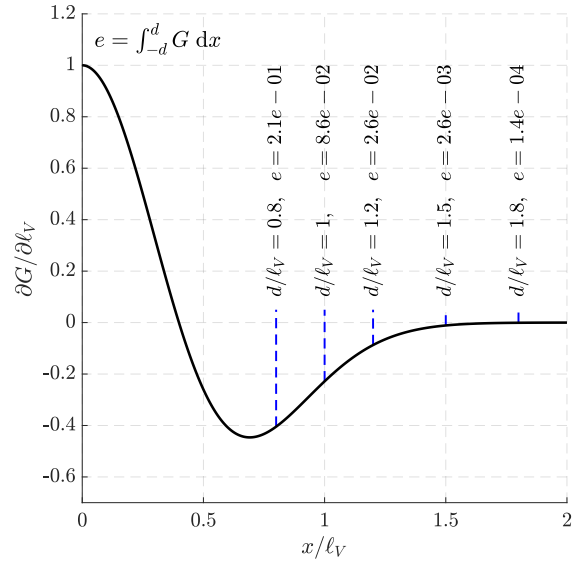
Results of the reference case were filtered on five uniform meshes with the element size

$$\frac{\Delta}{a} = \{0.2, 0.1, 0.05, 0.025\},$$

where a denotes the length of the side of the square. The residuals were again evaluated for every mesh and they are presented in Figure 21a. The mesh size of $\Delta/a = 0.05$ was selected as appropriate resolution for case G1-C as it reduced all error terms below 1% and the evaluated source terms did not change significantly on the finer mesh (Figure 21b). Interestingly the maximum of continuity residual increased slightly when the finest mesh was used. The reason for such behaviour is



(a) Gaussian filter



(b) derivative of the Gaussian filter with respect to filter width ℓ_V

FIG. 19. Depiction of the clipped filter shapes used in the sensitivity study. At chosen distance from the center d/ℓ_V kernel is clipped to 0. This threshold is shown in the figures by the blue dashed lines. Each value of d/ℓ_V is paired with corresponding value of the clipping error.

probably the fact that the resolution of the filtering mesh is finer in most of the domain than the source mesh.

REFERENCES

- ¹P. Sagaut, *Large eddy simulation for incompressible flows: an introduction*, 3rd ed., Scientific computation (Springer, 2006).
- ²C. Fureby and G. Tabor, “Mathematical and physical constraints on large-eddy simulations,” *Theoretical and Computational Fluid Dynamics* **9**, 85–102 (1997).
- ³O. V. Vasilyev and D. E. Goldstein, “Local spectrum of commutation error in large eddy simulations,” *Phys. Fluids* **16**, 5 (2004).
- ⁴N. Jurtz, M. Kraume, and G. D. Wehinger, “Advances in fixed-bed reactor modeling using particle-resolved computational fluid dynamics (cfD),” *Reviews in Chemical Engineering* **35**, 139–190 (2019).
- ⁵A. G. Dixon and B. Partopour, “Computational fluid dynamics for fixed bed reactor design,”

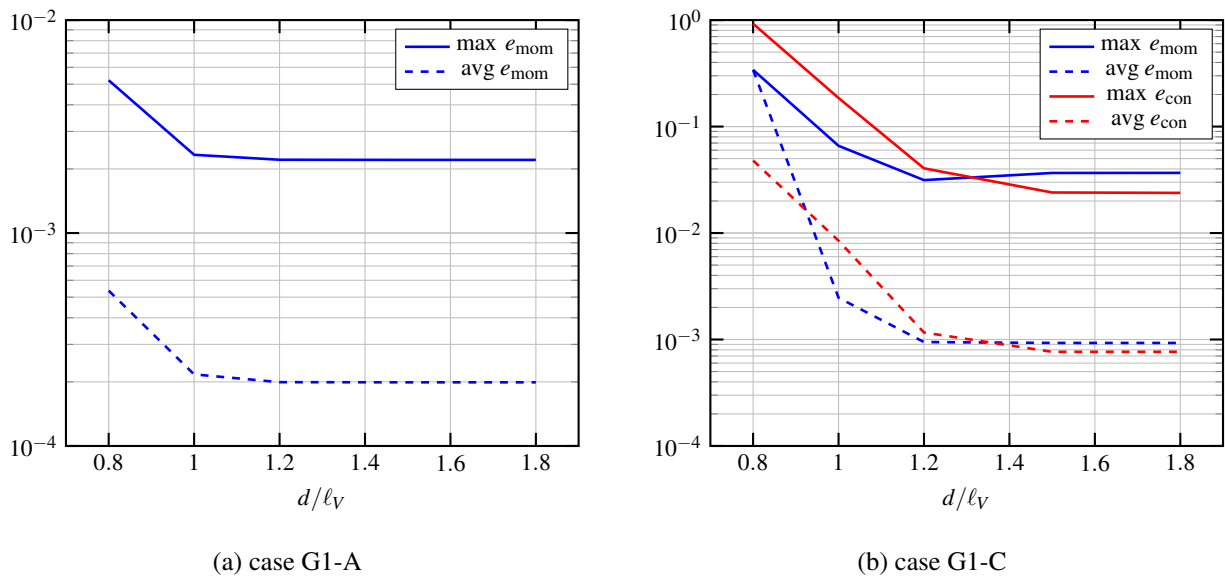
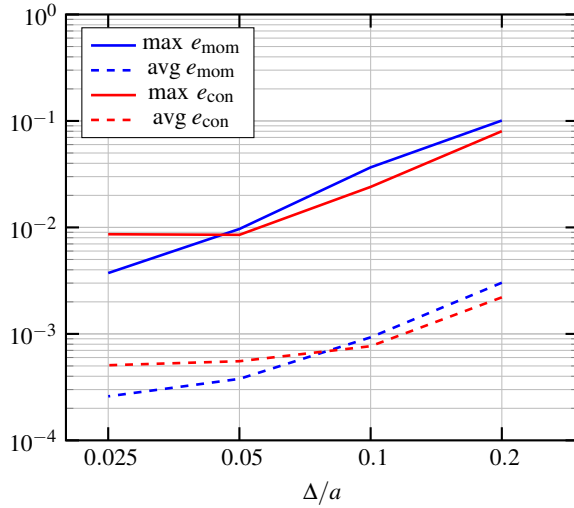


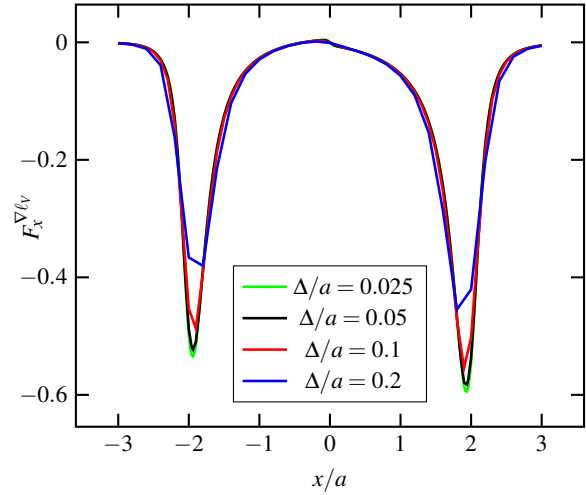
FIG. 20. Values of the maxima and averages of the residuals of momentum e_{mom} and continuity equation e_{con} of DANS system. The residuals were computed evaluating the balance of explicitly filtered terms of the both equations and are plotted against the filter clipping distance d/ℓ_V .

Annual Review of Chemical and Biomolecular Engineering **11**, 109–130 (2020).

- ⁶J. Collazo, J. Porteiro, D. Patiño, and E. Granada, “Numerical modeling of the combustion of densified wood under fixed-bed conditions,” *Fuel* **93**, 149–159 (2012).
- ⁷S. Woudberg and Éric Dumont, “Chapter 4 - porous media models for packed bed characterization,” in *From Biofiltration to Promising Options in Gaseous Fluxes Biotreatment*, edited by G. Soreanu and Éric Dumont (Elsevier, 2020) pp. 71–87.
- ⁸E. I. Mahiques, M. Brömmer, S. Wirtz, and V. Scherer, “Locally resolved simulation of gas mixing and combustion inside static and moving particle assemblies,” *Chemical Engineering & Technology* (2023), <https://doi.org/10.1002/ceat.202200622>.
- ⁹A. Shams, F. Roelofs, E. Komen, and E. Baglietto, “Optimization of a pebble bed configuration for quasi-direct numerical simulation,” *Nuclear Engineering and Design* **242**, 331–340 (2012).
- ¹⁰A. Shams, F. Roelofs, E. Komen, and E. Baglietto, “Numerical simulations of a pebble bed configuration using hybrid (RANS–LES) methods,” *Nuclear Engineering and Design* **261**, 201–211 (2013).
- ¹¹A. Shams, F. Roelofs, E. Komen, and E. Baglietto, “Quasi-direct numerical simulation of a pebble bed configuration. Part I: Flow (velocity) field analysis,” *Nuclear Engineering and Design* **263**, 473–489 (2013).



(a) residual values against the filtering mesh resolution, where Δ denotes the element size and a is the size of the square



(b) plots of the x component of the commutation error from inhomogenous filtering along the x axis in case G1-C

FIG. 21. Results of the filtering mesh sensitivity study.

- ¹²A. Shams, F. Roelofs, E. Komen, and E. Baglietto, “Large eddy simulation of a nuclear pebble bed configuration,” *Nuclear Engineering and Design* **261**, 10–19 (2013).
- ¹³A. Shams, F. Roelofs, E. Komen, and E. Baglietto, “Quasi-direct numerical simulation of a pebble bed configuration, part-ii: Temperature field analysis,” *Nuclear Engineering and Design* **263**, 490–499 (2013).
- ¹⁴A. Shams, F. Roelofs, E. Komen, and E. Baglietto, “Large eddy simulation of a randomly stacked nuclear pebble bed,” *Computers & Fluids* **96**, 302–321 (2014).
- ¹⁵A. Shams, F. Roelofs, E. Komen, and E. Baglietto, “Improved delayed detached eddy simulation of a randomly stacked nuclear pebble bed,” *Computers & Fluids* **122**, 12–25 (2015).
- ¹⁶J. Wiese, F. Wissing, D. Höhner, S. Wirtz, V. Scherer, U. Ley, and H. M. Behr, “DEM/CFD modeling of the fuel conversion in a pellet stove,” *Fuel Processing Technology* **152**, 223–239 (2016).
- ¹⁷S. Whitaker, “The Forchheimer equation: A theoretical development,” *Transport in Porous Media* **25**, 27–61 (1996).
- ¹⁸S. Ergun, “Fluid flow through packed columns chemical engineering progress vol. 48,” (1952).
- ¹⁹J. Ochoa-Tapia and S. Whitaker, “Momentum transfer at the boundary between a porous medium and a homogeneous fluid-i. theoretical development,” *International Journal of Heat and Mass*

- Transfer , 2635–2646 (1995).
- ²⁰J. Porteiro, J. Collazo, D. Patiño, E. Granada, J. C. Moran Gonzalez, and J. L. Míguez, “Numerical modeling of a biomass pellet domestic boiler,” *Energy & Fuels* **23**, 1067–1075 (2009).
- ²¹J. Rajika and M. Narayana, “Modelling and simulation of wood chip combustion in a hot air generator system,” *SpringerPlus* **5** (2016), 10.1186/s40064-016-2817-x.
- ²²N. Fernando and M. Narayana, “A comprehensive two dimensional computational fluid dynamics model for an updraft biomass gasifier,” *Renewable Energy* **99**, 698–710 (2016).
- ²³S. Whitaker, *The Method of Volume Averaging*, edited by J. Bear, Theory and Applications of Transport in Porous Media, Vol. 13 (Springer Netherlands, Dordrecht, 1999).
- ²⁴S. Whitaker, “Flow in porous media I: A theoretical derivation of Darcy’s law,” *Transport in Porous Media* **1**, 3–25 (1986).
- ²⁵S. Whitaker, “Flow in porous media II: The governing equations for immiscible, two-phase flow,” *Transport in Porous Media* **1**, 105–125 (1986).
- ²⁶B. Goyeau, D. Lhuillier, D. Gobin, and M. Velarde, “Momentum transport at a fluid–porous interface,” *International Journal of Heat and Mass Transfer* **46**, 4071–4081 (2003).
- ²⁷J. Lage, M. J. de Lemos, and D. Nield, “8 - modeling turbulence in porous media,” in *Transport Phenomena in Porous Media II*, edited by D. B. Ingham and I. Pop (Pergamon, Oxford, 2002) pp. 198–230.
- ²⁸V. Nikora, I. McEwan, S. McLean, S. Coleman, D. Pokrajac, and R. Walters, “Double-averaging concept for rough-bed open-channel and overland flows: Theoretical background,” *Journal of Hydraulic Engineering* **133**, 873–883 (2007).
- ²⁹V. Nikora, F. Ballio, S. Coleman, and D. Pokrajac, “Spatially averaged flows over mobile rough beds: Definitions, averaging theorems, and conservation equations,” *Journal of Hydraulic Engineering* **139**, 803–811 (2013).
- ³⁰K. Papadopoulos, V. Nikora, S. Cameron, M. Stewart, and C. Gibbins, “Spatially-averaged flows over mobile rough beds: equations for the second-order velocity moments,” *Journal of Hydraulic Research* **58**, 133–151 (2020).
- ³¹W. G. Gray, “A derivation of the equations for multi-phase transport,” *Chemical Engineering Science* **30**, 229–233 (1975).
- ³²B. Vowinckel, V. Nikora, T. Kempe, and J. Fröhlich, “Momentum balance in flows over mobile granular beds: application of double-averaging methodology to DNS data,” *Journal of Hydraulic Research* **55**, 190–207 (2017).

- ³³D. C. Wilcox, *Turbulence modelling for CFD* (DCW Industries, La Cañada, 1993).
- ³⁴W. G. Gray, “Local volume averaging of multiphase systems using a non-constant averaging volume,” *International Journal of Multiphase Flow* **9**, 755–761 (1983).
- ³⁵K. Papadopoulos, V. Nikora, B. Vowinckel, S. Cameron, R. Jain, M. Stewart, C. Gibbins, and J. Fröhlich, “Double-averaged kinetic energy budgets in flows over mobile granular beds: insights from DNS data analysis,” *Journal of Hydraulic Research* **58**, 653–672 (2020).
- ³⁶M. Iovieno and D. Tordella, “Variable scale filtered navier–stokes equations: a new procedure to deal with the associated commutation error,” *Physics of Fluids* **15**, 1926–1936 (2003).
- ³⁷M. Klein and M. Germano, “Analysis and Modelling of the Commutation Error,” *Fluids* **6**, 15 (2020).
- ³⁸A. Faghri and Y. Zhang, *Fundamentals of Multiphase Heat Transfer and Flow* (Springer International Publishing, Cham, 2020).
- ³⁹W. P. Breugem, B. J. Boersma, and R. E. Uittenbogaard, “The influence of wall permeability on turbulent channel flow,” *Journal of Fluid Mechanics* **562**, 35 (2006).
- ⁴⁰W. Sadowski and F. di Mare, “Investigation of the porous drag and permeability at the porous-fluid interface: Influence of the filtering parameters on darcy closure,” *Particuology* **78**, 122–135 (2023).
- ⁴¹M. Quintard and S. Whitaker, “Transport in ordered and disordered porous media II: Generalized volume averaging,” *Transport in Porous Media* **14**, 179–206 (1994).
- ⁴²W.-P. Breugem, *The influence of wall permeability on laminar and turbulent flows, Theory and simulations*, Doctoral, TU Delft, Delft (2005).
- ⁴³J. Bardino, J. H. Ferziger, and W. C. Reynolds, “Improved turbulence models based on large eddy simulation of homogeneous, incompressible turbulent flows,” Tech. Rep. (1983) publication Title: Stanford Univ. Report ADS Bibcode: 1983stan.reptV...B.
- ⁴⁴S. Irmay, “Modèles théoriques d’écoulement dans les corps poreux,” *bulletin Rilem* **29**, 37–45 (1965).
- ⁴⁵W. P. Breugem, B. J. Boersma, and R. E. Uittenbogaard, “Direct Numerical Simulations of plane channel flow over a 3d cartesian grid of cubes,” in *Proceedings of ICAPM 2004* (2004).
- ⁴⁶Y. Jin, M.-F. Uth, A. V. Kuznetsov, and H. Herwig, “Numerical investigation of the possibility of macroscopic turbulence in porous media: a direct numerical simulation study,” *Journal of Fluid Mechanics* **766**, 76–103 (2015).
- ⁴⁷F. Moukalled, L. Mangani, and M. Darwish, *The Finite Volume Method in Computational Fluid*

- Dynamics: An Advanced Introduction with OpenFOAM and Matlab*, Fluid Mechanics and Its Applications, Vol. 113 (Springer International Publishing, Cham, 2016).
- ⁴⁸H. Weller, G. Tabor, H. Jasak, and C. Fureby, “A tensorial approach to computational continuum mechanics using object orientated techniques,” *Computers in Physics* **12**, 620–631 (1998).
- ⁴⁹H. Jasak, *Error Analysis and Estimation for the Finite Volume Method with Applications to Fluid Flows*, Doctoral, Imperial College London (1996).
- ⁵⁰S. V. Patankar and D. B. Spalding, “A calculation procedure for heat, mass and momentum transfer in three-dimensional parabolic flows,” *International Journal of Heat and Mass Transfer* **15**, 1787–1806 (1972).
- ⁵¹F. Nicoud and F. Ducros, “Subgrid-Scale Stress Modelling Based on the Square of the Velocity Gradient Tensor,” , 18 (1999).
- ⁵²F. di Mare, R. Knappstein, and M. Baumann, “Application of les-quality criteria to internal combustion engine flows,” *Computers & Fluids* **89**, 200–213 (2014).
- ⁵³I. B. Celik, Z. N. Cehreli, and I. Yavuz, “Index of resolution quality for large eddy simulations,” **127**, 949–958 (2005).
- ⁵⁴D. R. Chapman, “Computational Aerodynamics Development and Outlook,” *AIAA Journal* **17**, 1293–1313 (1979).
- ⁵⁵Y. Kuwata and K. Suga, “Lattice boltzmann direct numerical simulation of interface turbulence over porous and rough walls,” **61**, 145–157 (2016).
- ⁵⁶R. A. Silva and M. J. de Lemos, “Turbulent flow in a channel occupied by a porous layer considering the stress jump at the interface,” *International Journal of Heat and Mass Transfer* **46**, 5113–5121 (2003).
- ⁵⁷S. Whitaker, “A simple geometrical derivation of the spatial averaging theorem,” *Chemical Engineering Education* , 8 (1985).
- ⁵⁸F. A. Howes and S. Whitaker, “The spatial averaging theorem revisited,” *Chemical Engineering Science* **40**, 1387–1392 (1985).
- ⁵⁹W. Gray and P. Lee, “On the theorems for local volume averaging of multiphase systems,” *International Journal of Multiphase Flow* **3**, 333–340 (1977).
- ⁶⁰I. P. Kinnmark and W. G. Gray, “An exposition of the distribution function used in proving the averaging theorems for multiphase flow,” *Advances in Water Resources* **7**, 113–115 (1984).
- ⁶¹L. Wang, L.-P. Wang, Z. Guo, and J. Mi, “Volume-averaged macroscopic equation for fluid flow in moving porous media,” *International Journal of Heat and Mass Transfer* **82**, 357–368 (2015).